To the Graduate Council:

I am submitting herewith a thesis written by Robert John Butler entitled "Boundary Layer Transition on Reentry Vehicle Nosetips." I have examined the final copy of this thesis for form and content and recommend that it be accepted in partial fulfillment of the requirements for the degree of Master of Science, with a major in Aerospace Engineering.

Roger A. Crawford

Roger A. Crawford, Major Professor

We have read this thesis
and recommend its acceptance:

Carroll E. Peters

Edward M. Kraft

Accepted for the Council:

C. W. Minkel

Vice Provost
and Dean of the Graduate School

STATEMENT OF PERMISSION TO USE

In presenting this thesis in partial fulfillment of the requirements for a Master's degree at The University of Tennessee, Knoxville, I agree that the Library shall make it available to borrowers under rules of the Library. Brief quotations from this thesis are allowable without special permission, provided that accurate acknowledgment of the source is made.

Permission for extensive quotation from or reproduction of this thesis may be granted by my major professor, or in his absence, by the Head of Interlibrary Services when, in the opinion of either, the proposed use of the material is for scholarly purposes. Any copying or use of the material in this thesis for financial gain shall not be allowed without my written permission.

Signature Robert J Butler

Date 24 Mar 89

BOUNDARY LAYER TRANSITION
ON REENTRY VEHICLE NOSETIPS

A Thesis
Presented for the
Master of Science
Degree
The University of Tennessee, Knoxville

Robert John Butler

May 1989

ACKNOWLEDGMENT

The author wishes to acknowledge the many personnel whose assistance was instrumental in the conduction of the experimental work and in the preparation of this thesis. The author would first like to thank Maj Wester for the management support required for the completion of this effort. The author is particularly indebted to Emmett Edenfield and Jim Blanks for their technical expertise in the subject of RV boundary layer transition. Furthermore, the advisory support provided by Dr. Crawford, Dr. Kraft, and Dr. Peters was outstanding. And finally, this project would have come to a standstill without the secretarial help from Kathy Swanson, Kathy Green, and Carol Pratt. Thanks.

ABSTRACT

Predicting reentry vehicle (RV) performance is a very difficult task and requires a detailed understanding of the nosetip boundary layer. Nosetip boundary layer transition typically occurs between 70,000 and 40,000 feet altitude and is a complex hypersonic fluid mechanics process that depends on surface roughness, wall temperature, nosetip geometry, and freestream conditions. The state of the boundary layer drives the ablation characteristics of the nosetip, which in turn, effects the vehicle performance. Therefore, accurate ground testing is vital in providing realistic RV preflight predictions.

The current work analyzes the transition studies completed by many authors and makes recommendations on which author's correlation best fits wind tunnel, ballistic range, arc tunnel, and flight data. Using the best correlation, a new data set encompassing ballistic range and arc tunnel data is compared and correlated. A simplified correlation is suggested to reconcile some differences between the arc and range data sets.

Furthermore, the study was enhanced by looking at the boundary layer problem using a linear stability model and a Reynolds number theoretical approach.

TABLE OF CONTENTS

CHAPTER PAGE

LIST OF TABLES

LIST OF FIGURES

FIGURE PAGE

FIGURE	PAGE

LIST OF SYMBOLS

a	Static Speed of Sound
C	Any Constant
C_p	Specific Heat at Constant Pressure
D	RV Nosetip Diameter
F	Dimensionless Frequency
H_B	Bulk Enthalpy
H_I	Enthalpy of Air Injected into Arc Heater
H_{INF}	Inferred Enthalpy
H_t	Total Enthalpy
h_{30}	Thirty Percent Exceedance Height
K	Material Roughness
K_{INF}	Inferred Material Roughness
K_{30}	Thirty Percent Exceedance Material Roughness Height
M	Mach Number
M_e	Mach Number at Edge of Boundary Layer
$\dot{M}_T$	Mass Flow of Air Injected into Arc Heater
P	Pressure
P_{ch}	Chamber Pressure of Arc Heater
P_e	Pressure at the Edge of Boundary Layer
P'_o	Total Pressure behind the Shock Wave
P_t	Total Pressure
P_w	Pressure at the Nosetip Wall
PWR_{IN}	Power Supplied to Arc Heater
PWR_L	Power Lost in Cooling Water

$\dot{Q}_o$	Heat Flux
R	Blasius Length Reynold's Number
Re	Reynold's Number
Re_k	Reynold's Number at the Peak of Material Roughness
Re_Θ	Momentum Thickness Reynold's Number
$Re_{\Theta T}$	Transition Momentum Thickness Reynold's Number
R_n	Nosetip Radius
S	Streamlength
$\dot{s}$	Recession Rate
S_{TR}	Transition Streamlength
T	Temperature
T_e	Temperature at Edge of Boundary Layer
T_t	Total Temperature
T_w	Temperature on the Wall of the Nosetip
u	Velocity
u*	Dimensional Velocity
U_e	Velocity at the Edge of the Boundary Layer
U_k	Velocity at the Peak of Material Roughness
X*	Dimensional Length
y_{ho}	Reference Height Determined from Exceedance Curve
y_o	Arbitrary Reference Height
y_s	Surface Height
γ	Ratio of Specific Heats
Θ	Momentum Thickness
ρ	Density
ρ_e	Density at the Edge of the Boundary Layer

ρ_k	Density at the Peak of Material Roughness
ρ_w	Density at the Nosetip Wall
ρ^*	Dimensional Density
ω	Nondimensional Frequency
ω^*	Dimensional Frequency
μ	Absolute Viscosity
μ_e	Absolute Viscosity at the Edge of the Boundary Layer
μ_k	Absolute Viscosity at the Peak of Material Roughness
μ^*	Dimensional Absolute Viscosity
v^*	Dimensional Kinematic Viscosity

CHAPTER I

INTRODUCTION

Thirty years of missile development has focused attention on the reentry vehicle (RV) nosetip and its aerodynamic boundary layer. During the 1960s, RV survival was the major concern; thus, the associated nosetip boundary layer and heat transfer rates were of considerable importance. Since new carbon-carbon composite materials were developed, the emphasis has shifted to understanding the boundary layer and predicting when and where transition will occur to improve the accuracy of future RV's. The current work analyzes the transition studies completed by many authors and makes recommendations on which correlation best fits wind tunnel, ballistic range, arc tunnel, and flight data. A new data set consisting of ballistic range and arc tunnel data is compared and correlated. In addition, ground testing techniques for future boundary layer transition experiments are suggested. Furthermore, the theoretical boundary layer problem is briefly examined.

Since the early seventies, many authors have predicted ground and flight test results using different correlations. Each of these works is briefly covered with concentration on the work of R. G. Batt and H. L. Legner [1], who proposed a method of predicting flight results using wind tunnel or ballistic range test data. The techniques used to acquire boundary layer transition data in the ballistic range and arc tunnel are reviewed. New carbon-carbon data sets produced in the ballistic range and arc tunnel are analyzed. Since I have proposed that the Batt and Legner correlation will fit the new data, a comparison is made. If in fact the arc tunnel data is an accurate simulation, in the future it could be used in a more quantitative manner and replace other types of ground testing.

In order to round out this study, the boundary layer transition problem was also looked at in a theoretical manner. Although solving the hypersonic boundary layer stability problem is beyond the scope of this paper, some methods examined produced results very similar to equivalant experimental correlations. Finally, the transition-inducing, unstable frequencies prevalent in the nosetip boundary layer were estimated to ensure that the same frequencies were not being produced by the arc tunnels in question.

CHAPTER II

BACKGROUND

For the past thirty years, the reentry community has tried to predict accurately ICBM reentry profiles, material ablation characteristics, and the inaccuracies involved with these processes. Typical ICBM reentry Mach numbers, enthalpies, stagnation point pressures, and heating rates are shown in Figure 1. Note that the maximum heating occurs at a fairly low altitude on the order of 40,000 feet. RV nosetip materials (graphites and carbon-carbon composites) sublimate under high heating rates forming a surface microroughness distribution characteristic of each material's composition and fabrication technique [14]. The nosetip surface roughness creates disturbances within the laminar boundary layer. As the RV altitude decreases and the Reynolds number increases, these disturbances amplify and the boundary layer undergoes transition to turbulent. Transition usually occurs between 70,000 and 40,000 feet altitude.

Now if we focus on the RV nosetip boundary layer, we can follow the ablation characteristics of the nosetip as shown in Figure 2. At high altitudes the boundary layer is laminar and the nosetip will tend to blunt itself, because the highest heating rate occurs at the stagnation point. As the RV flies lower, the boundary layer transition point

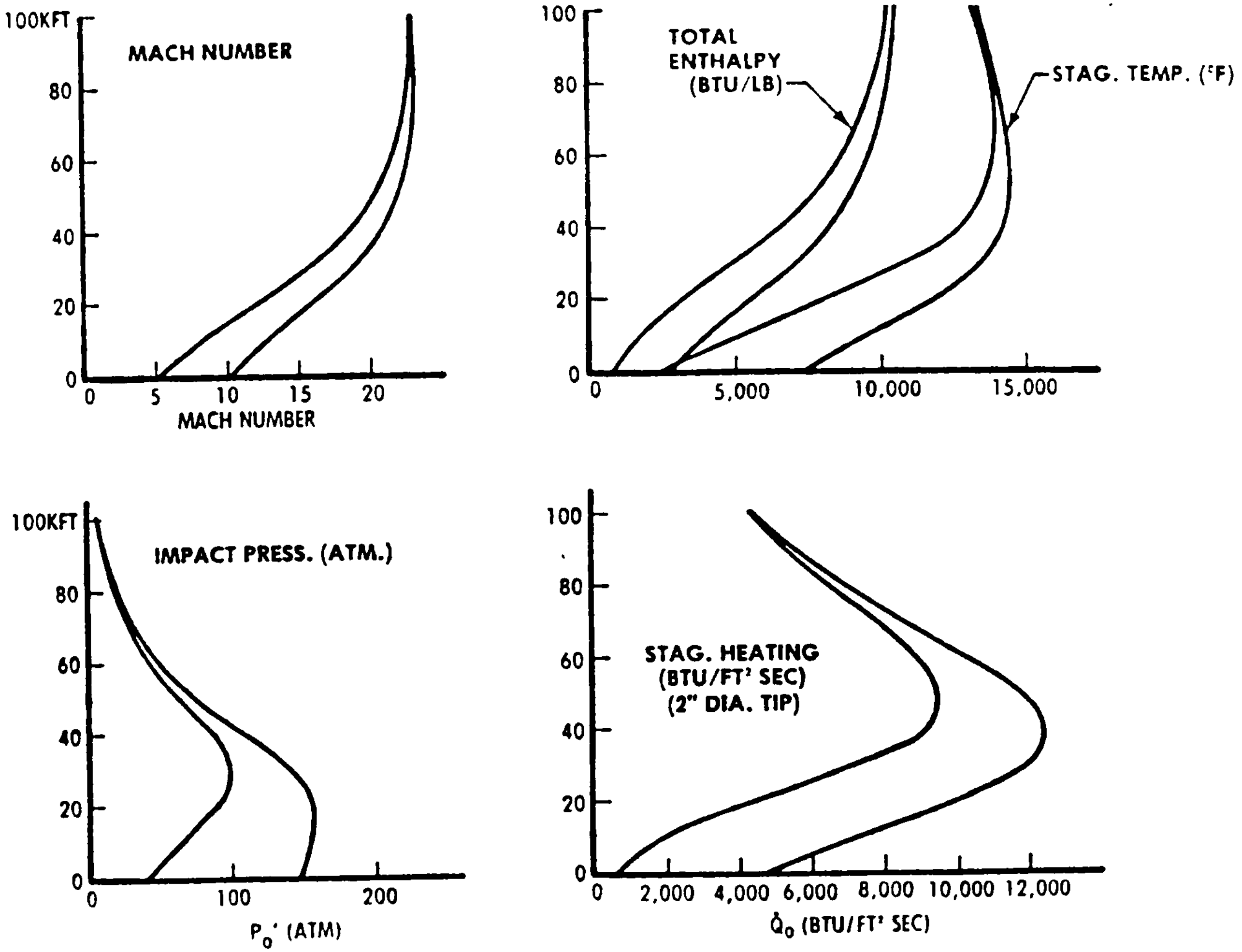

Figure 1. Typical ICBM Reentry Conditions

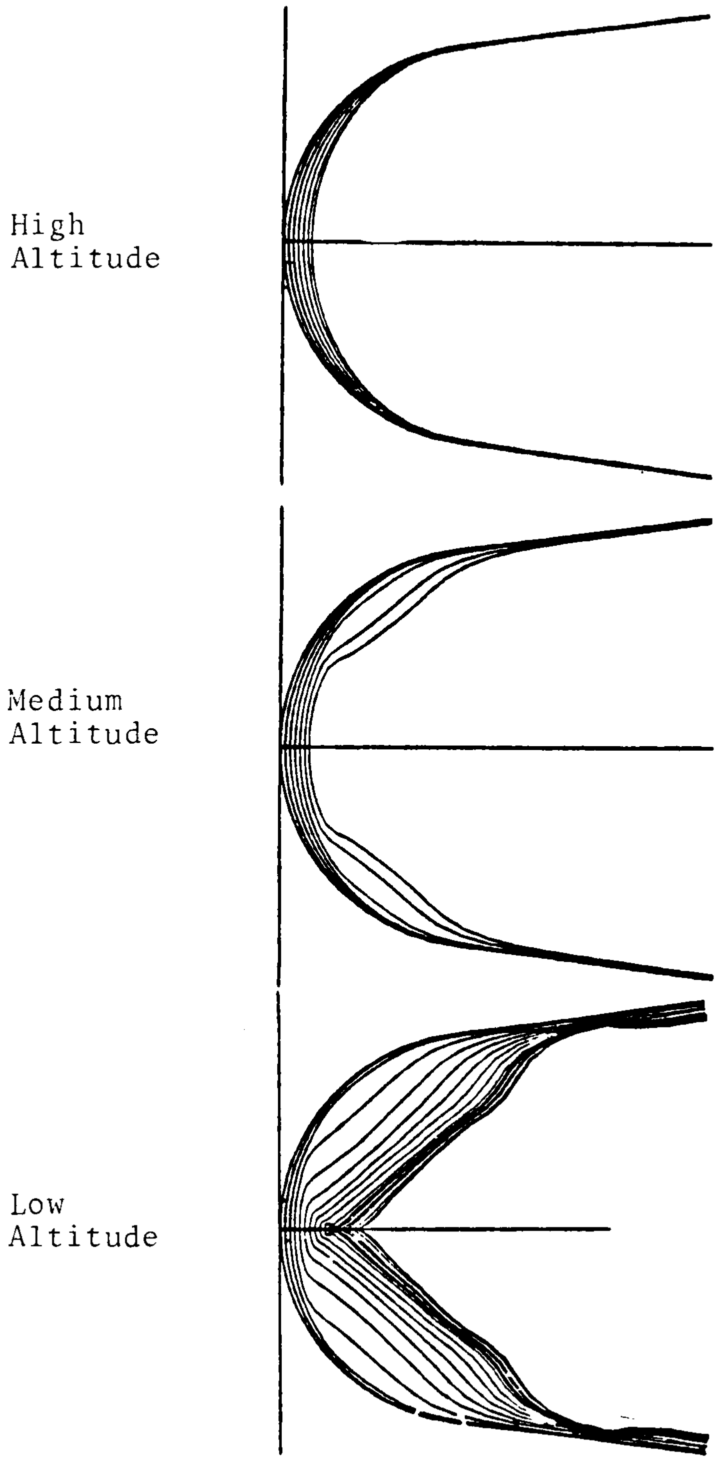

Figure 2. RV Nosetip Ablation Pattern

will move forward onto the nosetip just upstream of the sonic point. The turbulent boundary layer creates a more severe heat transfer, increased ablation rate, and accelerated shape change. This produces a nosetip shape which has a "laminar island" located around the stagnation point. Finally at low altitudes, the boundary layer is entirely turbulent and the nosetip forms a pointed cone, "fully turbulent shape." A recovered nosetip from the NRV flight test program [14] is shown in Figure 3. Notice the "laminar island" which has formed on this graphite nosetip.

Historically, the reentry concerns focused on RV survival. Thus, adequacy of thermal protection and heat transfer associated with the onset of transition were studied [2]. As technology progressed, ballistic vehicle targeting dispersion became a prime factor; therefore, how the turbulent boundary layer effects nosetip shape change is currently the driving factor in RV design. In this section, a review is made of past investigators who tried to model and predict when and where transition will occur on an RV nosetip and the effect on shape change. Reda [14] examined the work of many of these authors and compared their correlations with his ballistic-range data set.

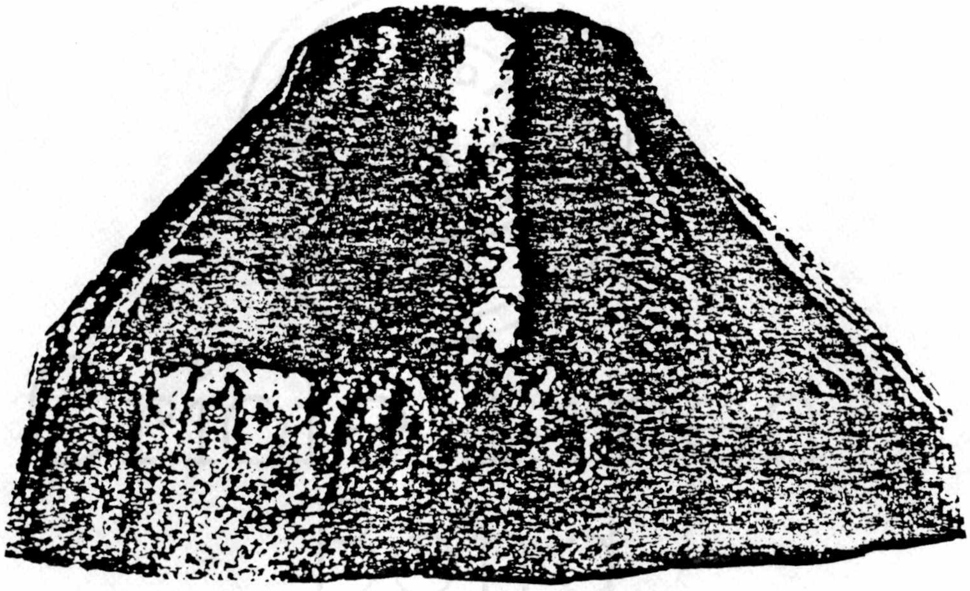

Figure 3. Recovered Flight Nosetip

Anderson

The Passive Nosetip Technology (PANT) Program [23] studied the nosetip boundary layer transition problem primarily in wind tunnel experiments conducted in the early seventies. In numerous wind tunnel experiments, different nosetips were examined with a variety of surface roughnesses, Mach numbers, temperatures, and pressures. The PANT database is the largest of its kind. Anderson is well known for developing the data correlation which predicted transition onset and progression from the PANT results [14]. His correlation is very similar to today's more refined formulas. It features many common factors such as the momentum thickness Reynolds number ($R_{e\theta}$), the material roughness height (k), the boundary layer momentum thickness (Θ), wall temperature (T_w), and boundary layer edge temperature (T_e). The Anderson correlation is:

$$R_{e\theta} = 215\left(\frac{Te}{Tw}\frac{k}{\theta}\right)^{-.7} \quad (1)$$

and is graphed in Figure 4. This correlation first showed that the nosetip surface roughness and the boundary layer momentum thickness were the driving factors in transition. In a physical sense, the material roughness can be thought to generate flow disturbances; as these disturbances grow larger, they start to interrupt the boundary layer and transition occurs. It is important to point out that

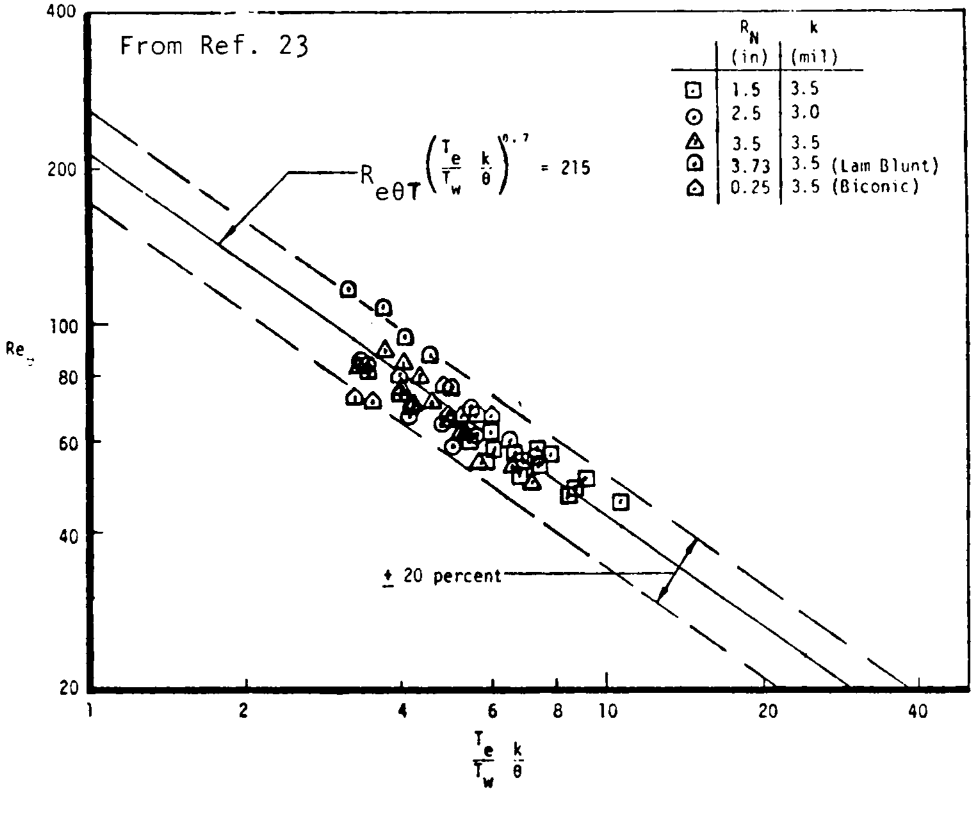

Figure 4. Anderson's Correlation

transition always occurred upstream of the sonic line in the subsonic region of the boundary layer. The PANT database included a very wide range of surface roughness values. Later we will find that the low surface roughness values tended to skew the data because of freestream disturbances in the wind tunnel flowfield [1]. With the low roughness data included, the Anderson correlation predicted transition too early and did not correctly predict transition progression (the slope of their curve was too shallow).

Van Driest

Van Driest [20] is well known for quantifying the stabilizing feature of the nosetip surface curvature. Van Driest provided technical comments on the PANT correlation which slightly modified Anderson's correlation [14]. He suggested that the material surface roughness (k) be divided by:

$$\left(1 + 350\,\frac{k}{Rn}\right) \qquad (2)$$

Notice that his modification shows the importance of the nosetip curvature radius (R_n). From his previous experience, Van Driest knew that the surface curvature provided a stabilizing influence on the boundary layer, because it induces a favorable pressure gradient. Van

Driest's curvature term will show up in many of the later correlations.

Bishop

Bishop divided the transition problem into two distinct regions. The first region of interest is where the flow strikes the stagnation point and makes a sharp turn (strong curvature) to follow the nosetip contour [14]. In the strong curvature region, the flow is dominated by streamwise (Goertler) vortices which are destabilizing. The second region (weak curvature), is dominated by the nosetip curvature radius (R_n) . We are most interested in the weak curvature region, where S/R_n > .3, because nosetip transition onset will first occur in this region. Bishop's correlation [3] for the weak curvature region is:

$$R_{e\theta}\left(1 + 4.5\,\frac{T_w}{T_e}\,M_e^{\,2}\right)^{-1/2} = 5.6\left(\frac{k}{2R_n}\right)^{-1/3} \qquad (3)$$

which is graphed in Figure 5. Note that the temperature ratio and most of the other terms are similar to the PANT correlation. However, Bishop includes the edge Mach number as a stabilizing influence to the boundary layer. Physically if the edge condition has a very high Mach number, a fluid particle near the wall wouldn't have the ability to significantly disturb the freestream flow [14]. Bishop defined his roughness height to be the roughness

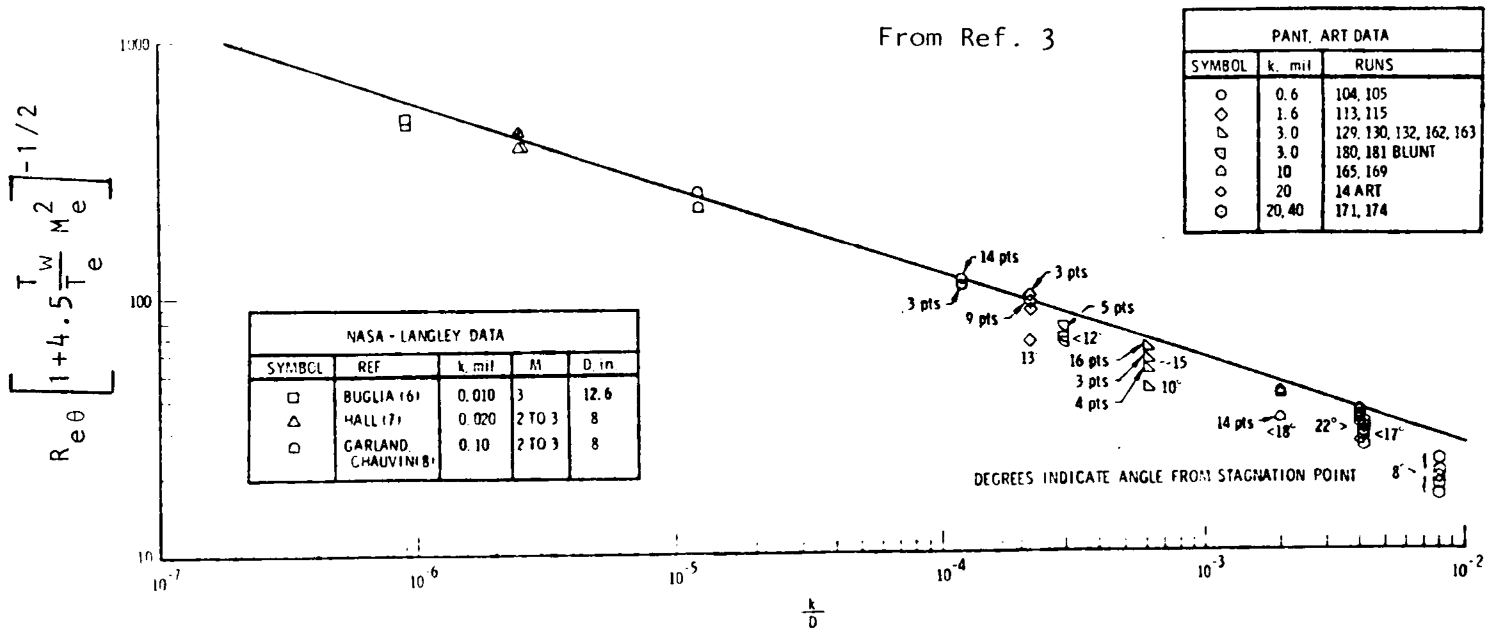

Figure 5. Bishop's Correlation

elements which have a roughness greater in height than 85 percent of the other elements [3]. This is interesting, because later we will find that the biggest problem associated with the early correlations was the inconsistent definition of the material roughness height.

Finson

During the middle seventies, Finson [7] listed the various parameters that were expected to influence nosetip transition and then investigated their influence. From Finson's analysis, he developed the correlation[7]:

$$R_{e\theta} = 3.5 \cdot 10^5 \left(1 + 1000 \frac{\theta}{R_n}\right)\left(R_{ek}\right)^{-1.64} \tag{4}$$

which is graphed in Figure 6. The material surface roughness parameter is not apparent, but exists in the surface roughness Reynolds number term. The other influencing terms, momentum thickness, nosetip curvature radius, and momentum thickness Reynolds number, are not new. Once again, the destabilizing influences are the momentum thickness and the momentum thickness Reynolds number, while Finson included his own variation on the stabilizing influence of the nosetip curvature.

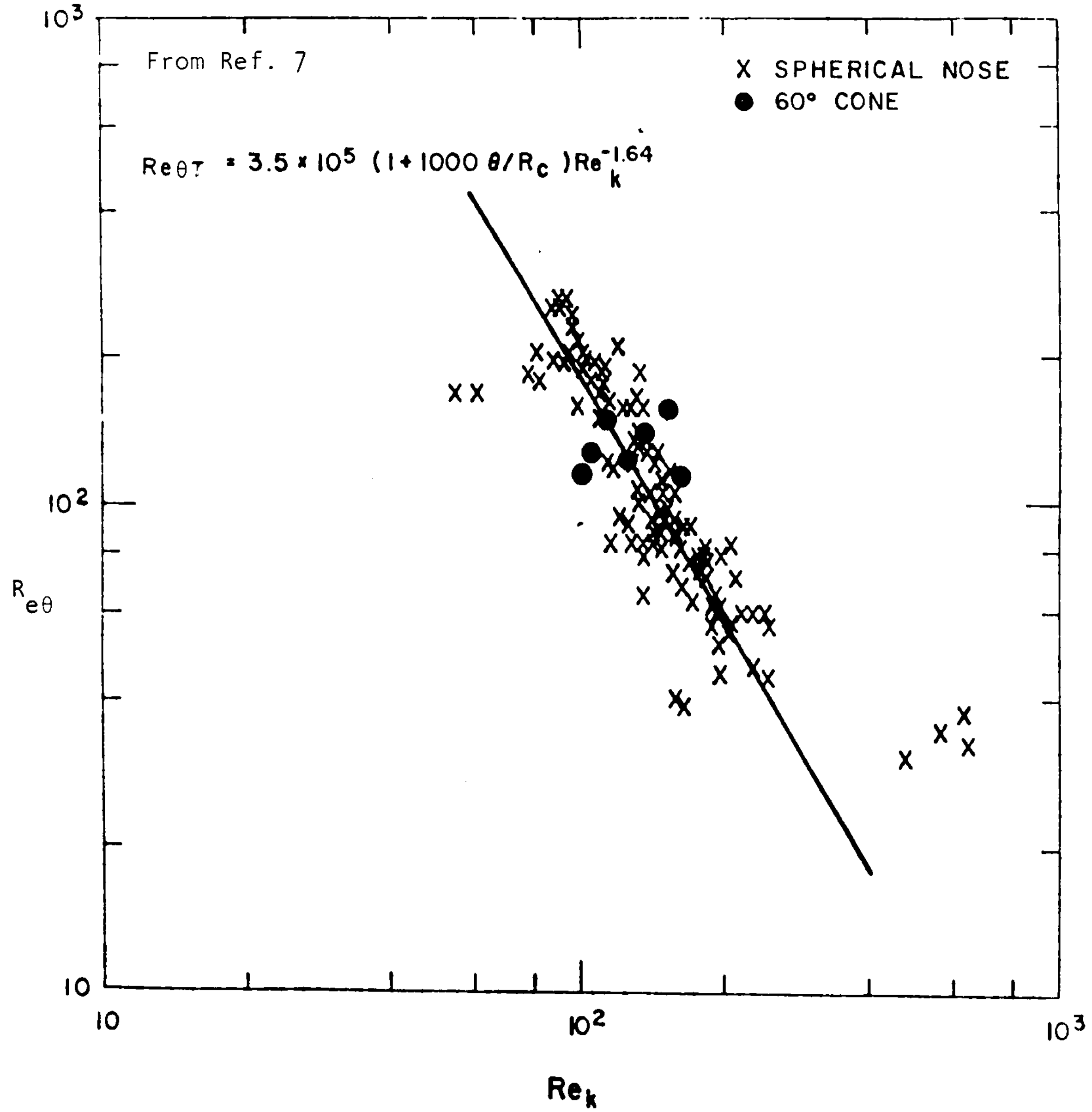

Figure 6. Finson's Correlation

Dirling

Dirling placed heavy emphasis on the surface roughness/momentum thickness ratio (k/θ) [5]. He studied the effects of this variable on the transition location and developed the following correlation:

$$R_{e\theta} = 160\left(\frac{\rho_k}{\rho_e}\frac{U_k}{U_e}\frac{k}{\theta}\right)^{-1.0} \qquad (5)$$

The Dirling correlation is graphed in Figure 7. It can be seen that the correlation is divided into two regions. First, where k is small, the boundary layer is not affected by the surface roughness and will undergo transition when the momentum thickness Reynolds number reaches 160. The momentum thickness Reynolds number of 160 is defined as the smooth wall limit [5]. The smooth wall limit is an important concept which will exist in the final correlation. The second region of importance is where the surface roughness is large and is the driving factor in the boundary layer. In this region, Dirling's formula is very similar to the PANT correlation but has a slightly steeper slope of -1.0. Dirling included the influence of the surface curvature by defining the surface roughness with the Van Driest's term included.

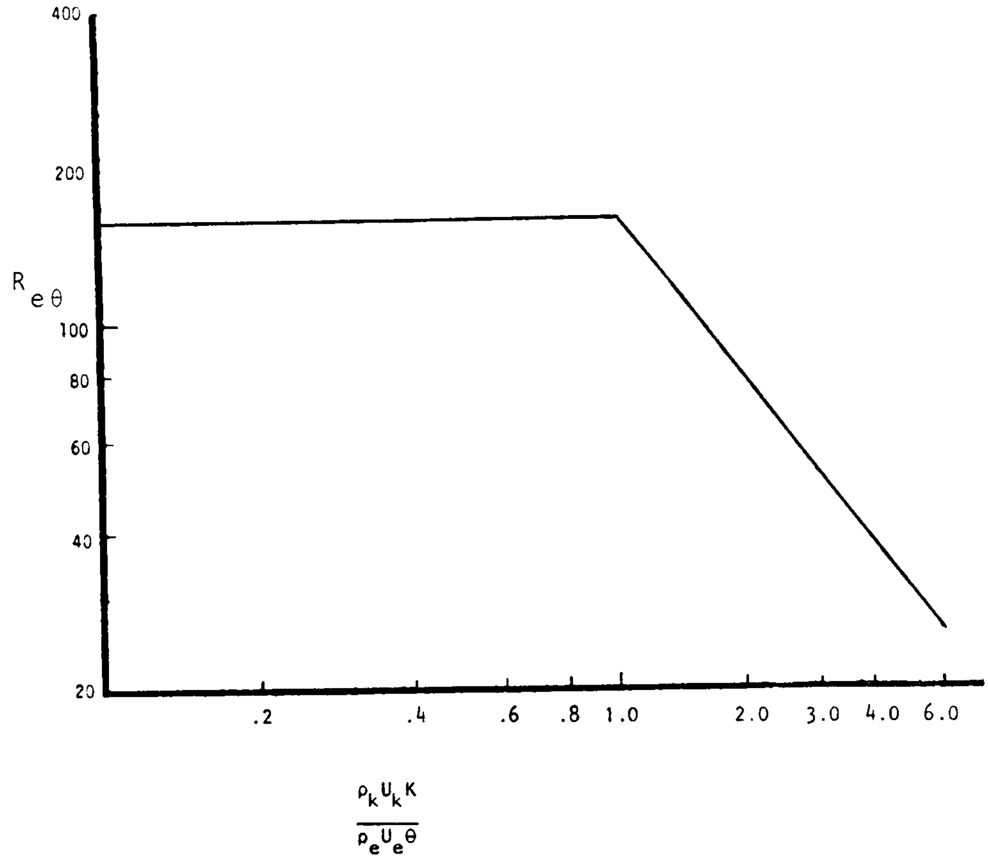

Figure 7. Dirling's Correlation

Demetriades

In the early eighties, Demetriades carried out a study on boundary layer transition by taking measurements on the inside of a supersonic nozzle and varying the surface roughness [4]. He showed that all the previous correlations predicted transition too early and did a poor job predicting transition onset at low surface roughnesses. Demetriades confirmed the theory of the smooth wall limit on the momentum thickness Reynolds number. His analysis showed the momentum thickness Reynold's number smooth wall limit to be 200. His work helped to explain why flight nosetips were undergoing transition at lower altitudes than expected.

Batt and Legner

The most comprehensive study was completed by Batt and Legner [1] using all the ground and flight test data available. They recognized a problem with the PANT database at low surface roughnesses. Freestream disturbances in the wind tunnels induced numerous shortcomings in the PANT database. First when the low surface roughness data was included, the correlations had too shallow of slope and did not predict transition progression correctly. Second, the wind tunnel freestream disturbances caused the boundary layer to undergo transition at low surface roughnesses which produced a correlation with a low smooth wall limit for the momentum thickness Reynolds number. It is the author's opinion that the most important part of Batt and Legner's analysis is their consistent use of the surface roughness. Past investigators used arbitrary or inconsistent roughness definitions. Batt and Legner took the known data and calculated consistent surface roughness values. Instead of trying to identify the complex element shape and spacing of the nosetip surface, they assumed that the larger roughness elements dominated the boundary layer. They quantified this by defining the 30 percent exceedence height (k_{30}) definition for the material roughness. They calculated the probability of exceedance curve for the individual roughness heights and determined the 30 percent value for each tested material. By making all the data sets consistent, Batt and Legner could analyze the data in a more accurate fashion. Batt and Legner's correlation is:

$$R_{e\theta} = 500 \left[\frac{k}{\theta} \frac{T_e}{T_w \left(1 + 350 \frac{k}{R_n} \right)} \right]^{-1.5} \qquad (6)$$

which is graphed in Figure 8. Their formula looks very similar to the past ones but differs in some respects. Note their smooth wall limit is 500, consistent with flight test values where freestream turbulence is not present. And their transition progression slope is -1.5, much steeper, because it is not influenced by the poor low

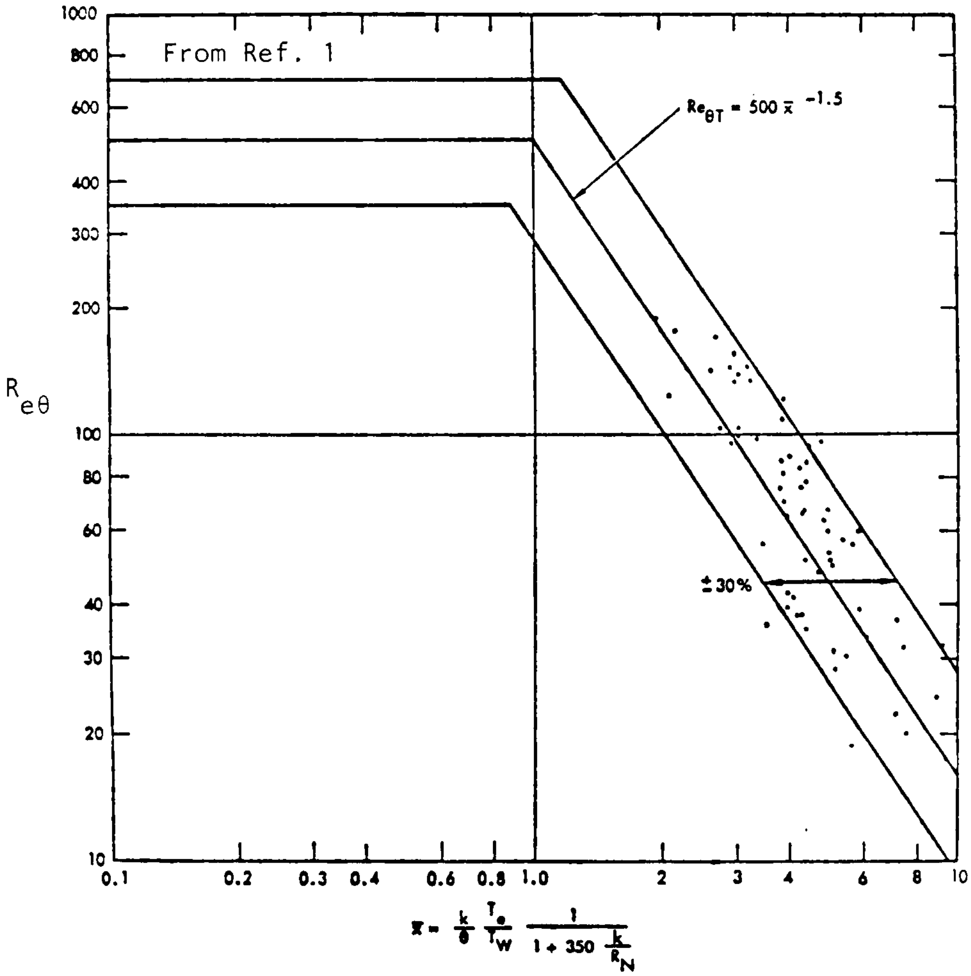

Figure 8. Batt and Legner's Correlation

roughness PANT data. Finally, they accounted for the nosetip curvature by using the now familiar Van Driest term.

In summary, the Batt and Legner correlation seems to be the most accurate work completed to date, and it will be used to analyze the new data sets.

CHAPTER III

THEORETICAL ANALYSIS

Although solving the boundary layer transition problem in a theoretical manner is beyond the scope of this paper, a linear stability theory example is considered to assure the arc tunnel test results are reasonable. Furthermore, a short theoretical transition analysis is performed. But first, we must understand the arc-tunnel flowfield with which we are concerned.

Flowfield

For the current analysis, consider the flowfield produced in a high temperature arc-heated wind tunnel. Arc-tunnel transition tests are typically performed at 100 Atm total pressure and 2500 Btu/Lbm total enthalpy. Using an underexpanded convex parabolic nozzle in a freejet tunnel, the flowfield will be at high pressure and low Mach number very near the nozzle exit; and the flow will expand to a higher Mach number and lower pressure away from the nozzle exit. Because high temperatures are produced in the flowfield by a rotating electrical arc, there are small fluctuations in the flowfield which occur at the same frequency of the arc rotation rate. The arc rotation rate is measured at about 250 Hz.

A typical transition model has a hemisperical nosetip which will produce a standoff normal shock wave as shown in Figure 9. Knowing the model location and the tunnel total conditions when transition occurs, one can calculate all the other flowfield properties. The freestream Mach number for transition onset is typically around three. For a rough-order-of-magnitude calculation, frozen flow with constant C_p and γ will be assumed. From [8], 6500 degrees Rankine air would have a C_p = .311 Btu/lb.R^o and γ = 1.25. Because the flow has a total enthalpy of 2500 Btu/Lbm, we know:

$$T_t = \frac{h_t}{C_p} = 8040^o R \qquad (7)$$

Knowing the total temperature and the Mach number, the freestream temperature, speed of sound, and velocity can be calculated.

$$T_1 = \frac{T_t}{(1 + \frac{\gamma - 1}{2} M^2)} = 3784^o R \qquad (8)$$

$$a_1 = (\gamma R T_1)^{1/2} = 2849 \, ft/s \qquad (9)$$

$$u_1 = M_1 \, a_1 = 8547 \, ft/s \qquad (10)$$

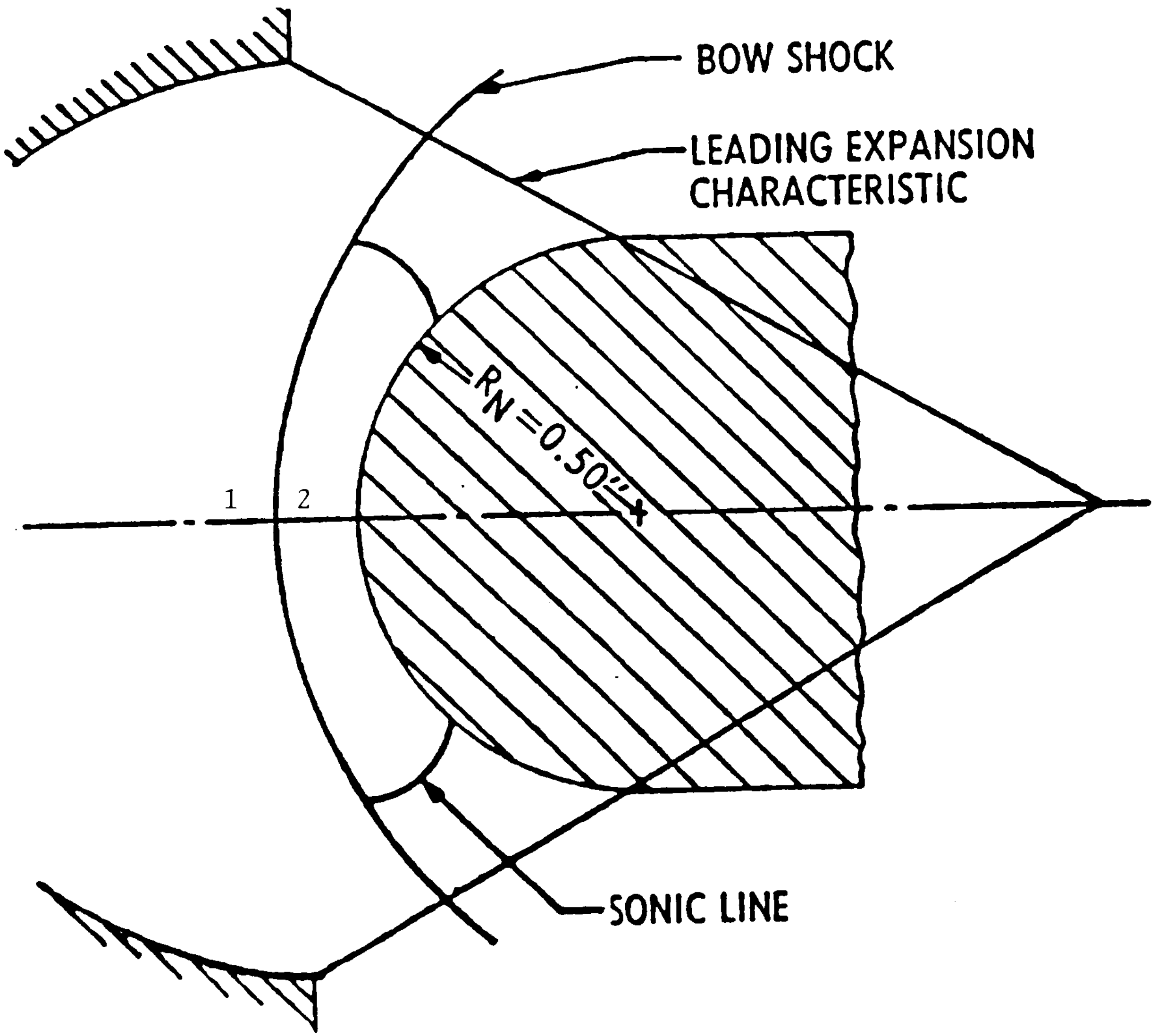

Figure 9. Nosetip in Arc Tunnel Flowfield

The total pressure of the tunnel is 100 Atm; therefore, using the isentropic relationship for pressures, the freestream pressure is calculated.

$$P_1 = \frac{P_{t1}}{(1 + \frac{\gamma - 1}{2} M^2)^{\gamma/\gamma - 1}} = 4{,}885\, psf \qquad (11)$$

The density is calculated by:

$$\rho_1 = \frac{P_1}{RT_1} = .00075 \frac{slug}{ft^3} \qquad (12)$$

Using the viscosity relationship in [19], the absolute viscosity can be determined.

$$\mu_1 = \left[.317 (T_1)^{1.5} \frac{734.7}{T_1 + 216} \right] 10^{-10} = 1.36 \cdot 10^{-6} \frac{slug}{ft \cdot s} \qquad (13)$$

Now that all the conditions upstream of the shock wave are known, the subsonic conditions behind the shock can be calculated using the normal shock relationships in [8].

$$M_2 = .435 \qquad (14)$$

$$P_2 = 9.9 P_1 = 48{,}362\, psf \qquad (15)$$

$$\rho_2 = 4.8\rho_1 = .0036 \frac{slug}{ft^3} \quad (16)$$

$$T_2 = 2.1T_1 = 7{,}946^o R \quad (17)$$

$$P_{t2} = .255\, P_{t1} = 53{,}978\, psf \quad (18)$$

Finally, the speed of sound, velocity, and viscosity can be determined in the subsonic region upstream of the stagnation point.

$$a_2 = (\gamma R T_2)^{1/2} = 4{,}128\, ft/s \quad (19)$$

$$U_2 = M_2 a_2 = 1{,}796\, ft/s \quad (20)$$

$$\mu_2 = \left[.317\,(T_2)^{1.5} \left(\frac{734.7}{T_2 + 216} \right) \right] 10^{-10} = 2.0 \cdot 10^{-6} \quad (21)$$

All the flowfield conditions are summarized in Table 1.

Linear Stability Theory

Mack in [12] used linear stability theory to address supersonic boundary layer transition. We will apply his technique to the arc-heated flowfield in order to calculate the frequency (order of magnitude) at which flow instabilities are prevalent in the flow. As mentioned earlier, an arc tunnel flowfield is considered very unsteady compared to cold tunnels. Although there is a lot

Table 1. Arc Tunnel Flowfield Properties

	Condition at 1	Condition at 2	Units
T	3,784	7,946	°R
T_t	8,040	8,040	°R
M	3.0	.435	--
a	2,849	4,128	ft/s
U	8,547	1,796	ft/s
P	4,885	48,362	psf
ρ	.00075	.0036	$\frac{slug}{ft^3}$
μ	$1.36 \cdot 10^{-6}$	$2.0 \cdot 10^{-6}$	$\frac{slug}{ft.s}$

to learn about arc-tunnel flow variations, it is known that the flowfield fluctuates at about the same frequency as the arc rotation rate. The arc rotation rate has been measured at about 250 Hz and will be compared to the unstable frequency in the nosetip boundary layer. Therefore, the unstable frequency for the flow upstream and downstream of the standoff shock wave needs to be calculated. Mack's analysis produced amplitude growth curves as shown in Figure 10. The parameters in Figure 10 are nondimensional and require some interpretation. We will concentrate on the dimensionless frequency (F), defined as:

$$F = \frac{\omega}{R} \tag{22}$$

In Equation 22, (ω) is the nondimensional freqency, and (R) is the square root of the Reynolds number. Mack uses starred notation to show dimensional quantities. We are interested in determining the dimensional frequency (ω^*). (ω) is defined as:

$$\omega = \frac{\omega^* X^*}{U_1^* R} \tag{23}$$

Therefore, substituting Equation 23 into Equation 22 yields:

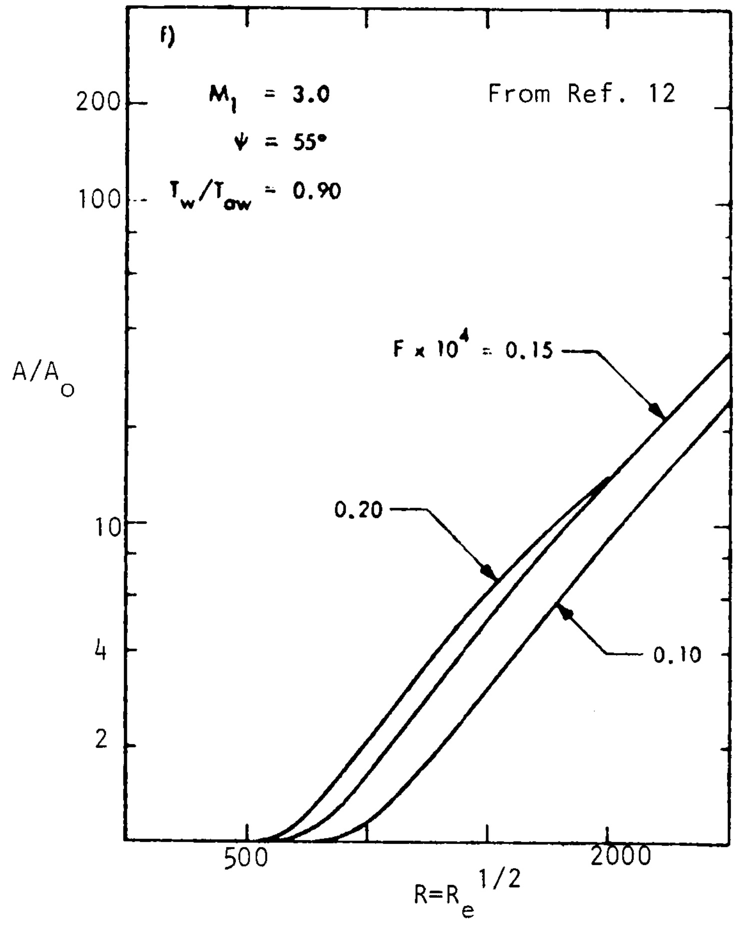

Figure 10. Mack's Amplitude Growth Curve

$$F = \frac{\omega^* X^*}{U_1^* R^2} \tag{24}$$

Now, knowing that:

$$R^2 = R_e = \frac{U_1^* X^*}{\nu_1^*} \tag{25}$$

substituting Equation 25 into Equation 24 produces:

$$F = \frac{\omega^* \nu_1^*}{(U_1^*)^2} \tag{26}$$

And finally, substituting absolute viscosity in for kinematic viscosity yields:

$$\nu_1^* = \frac{\mu_1^*}{\rho_1^*} \tag{27}$$

$$F = \frac{\omega^* \mu_1^*}{(U_1^*)^2 \rho_1^*} \tag{28}$$

Rearranging Equation 28 reveals the formula:

$$\omega^* = \frac{F (U_1^*)^2 \rho_1^*}{\mu_1^*} \tag{29}$$

Using the results shown in Table 1, the unstable frequency (order of magnitude) associated with the flowfield in front of and behind the standoff shock wave can be calculated.

$$\omega_1^* = \frac{1 \cdot 10^{-5} (U_1^*)^2 \rho_1^*}{\mu_1^*} = 403\, KHz \qquad (30)$$

$$\omega_2^* = \frac{1 \cdot 10^{-5} (U_2^*)^2 \rho_2^*}{\mu_2^*} = 58\, KHz \qquad (31)$$

As expected, using the lowest dimensionless frequency, the unstable frequencies in the boundary layer are several orders of magnitude higher than the known dominant fluctuations in the arc flowfield. Although this is an approximate analysis, it does show that flowfield disturbances are probably not a driving factor in the stability of the boundary layer.

Transition

Predicting RV nosetip transition at flight conditions using a theoretical calculation has proven difficult for all investigators. However, Batt and Legner [1] have suggested that advances can probably be made using the following type of analysis.

Two definitions for Reynolds number have been used for transition correlation by past investigators. They are the Reynolds number based on the material roughness height:

$$R_{ek} = \frac{\rho_k U_k k}{\mu_k} \tag{32}$$

and the Reynolds number based on the boundary layer momentum thickness:

$$R_{e\theta} = \frac{\rho_k U_e \Theta}{\mu_e} \tag{33}$$

Taking the ratio, we obtain:

$$R_{e\theta} = \frac{\Theta}{k} \frac{\rho_e}{\rho_k} \frac{\mu_k}{\mu_e} \frac{U_e}{U_k} R_{ek} \tag{34}$$

Expecting transition to occur at a critical roughness height yields a constant material roughness Reynolds number ($R_{ek} = C_1$). When this occurs, the momentum thickness Reynolds number would be designated with a subscript t and we would obtain:

$$R_{e\theta T} = C_1 \frac{\Theta}{k} \frac{\rho_e}{\rho_k} \frac{\mu_k}{\mu_e} \frac{U_e}{U_k} \tag{35}$$

Multiplying by (ρ_w/ρ_w) yields:

$$R_{e\theta T} = C_1 \frac{\Theta}{k} \frac{\rho_e}{\rho_w} \frac{\rho_w}{\rho_k} \frac{\mu_k}{\mu_e} \frac{U_e}{U_k} \tag{36}$$

From the perfect gas law, we know:

$$\frac{\rho_e}{\rho_w} = \frac{T_w}{T_e} \frac{P_e}{P_w} \tag{37}$$

Substituting Equation 37 into Equation 36 reveals:

$$R_{e\theta T} = C_1 \frac{\Theta}{k} \frac{T_w}{T_e} \frac{P_e}{P_w} \frac{\rho_w}{\rho_k} \frac{\mu_k}{\mu_e} \frac{U_e}{U_k} \tag{38}$$

Now multiplying by (ρ_e/ρ_e) yields:

$$R_{e\theta T} = C_1 \frac{\Theta}{k} \frac{T_w}{T_e} \frac{P_e}{P_w} \frac{\rho_w}{\rho_e} \frac{\rho_e}{\rho_k} \frac{\mu_k}{\mu_e} \frac{U_e}{U_k} \tag{39}$$

Examining the magnitude of (Θ) and (k), we can assume that (Θ/k) is roughly equal to one. This is a realistic assumption since current carbon-carbon composite materials have a roughness on the order of 1 mil. As (k) approaches (Θ), $U_k \rightarrow U_e$, $\mu_k \rightarrow \mu_e$, and $\rho_k \rightarrow \rho_e$. Therefore, Equation 39 can be reduced to:

$$R_{e\theta T} = C_1 \frac{\Theta}{k} \frac{T_w}{T_e} \frac{P_e}{P_w} \frac{\rho_w}{\rho_e} \tag{40}$$

From the perfect gas law, we know:

$$\frac{T_e}{T_w} = \frac{P_e}{P_w}\frac{\rho_w}{\rho_e} \tag{41}$$

Substituting Equation 41 into Equation 40, we obtain:

$$R_{e\theta T} = C_1 \frac{\Theta}{k}\frac{T_w}{T_e}\frac{T_e}{T_w} \tag{42}$$

Cancelling terms and rewriting in a familar manner yields:

$$R_{e\theta T} = C_1 \left(\frac{k}{\Theta}\right)^{-1.0} \tag{43}$$

This equation now looks very similar to the experimental correlations developed by earlier investigators. It is interesting to note that once again momentum thickness and surface roughness are the driving factors of the stability of the boundary layer. The -1.0 slope of this equation falls in between the values determined by Anderson (-.7), and Batt and Legner (-1.5). Equation 43 will be used in Chapter VI to produce a new data correlation which will help reconcile differences between arc and range transition data.

CHAPTER IV

ARC-HEATED TUNNEL TESTING

The arc-heated tunnel can provide data on transition behavior for realistic nosetip materials under conditions simulating the high enthalpy and pressure loadings of reentry [1]. In the past, inherent limitations in arc tunnel testing, such as freestream turbulence and measurement resolution, have required investigators to carefully qualify results. The arc results were primarily used to screen material samples to get a rough idea of their ablation rate and transition onset pressure. We will examine whether arc data can be used in a more quantitative manner to predict transition onset and progression. But first we must understand the arc tunnel flowfield and testing techniques.

Flowfield

The internal arc tunnel conditions were calculated in Chapter III. Using these total conditions and expanding the flow through an axisymmetric flared nozzle (convex parabolic contour from throat to exit) provides a test jet with a 1.38-inch exit diameter with a nominal exit Mach number of 1.9 (Figure 11). Because the gas is underexpanded and exits on a parabolic path, the flow will continue to expand as it passes downstream from the nozzle

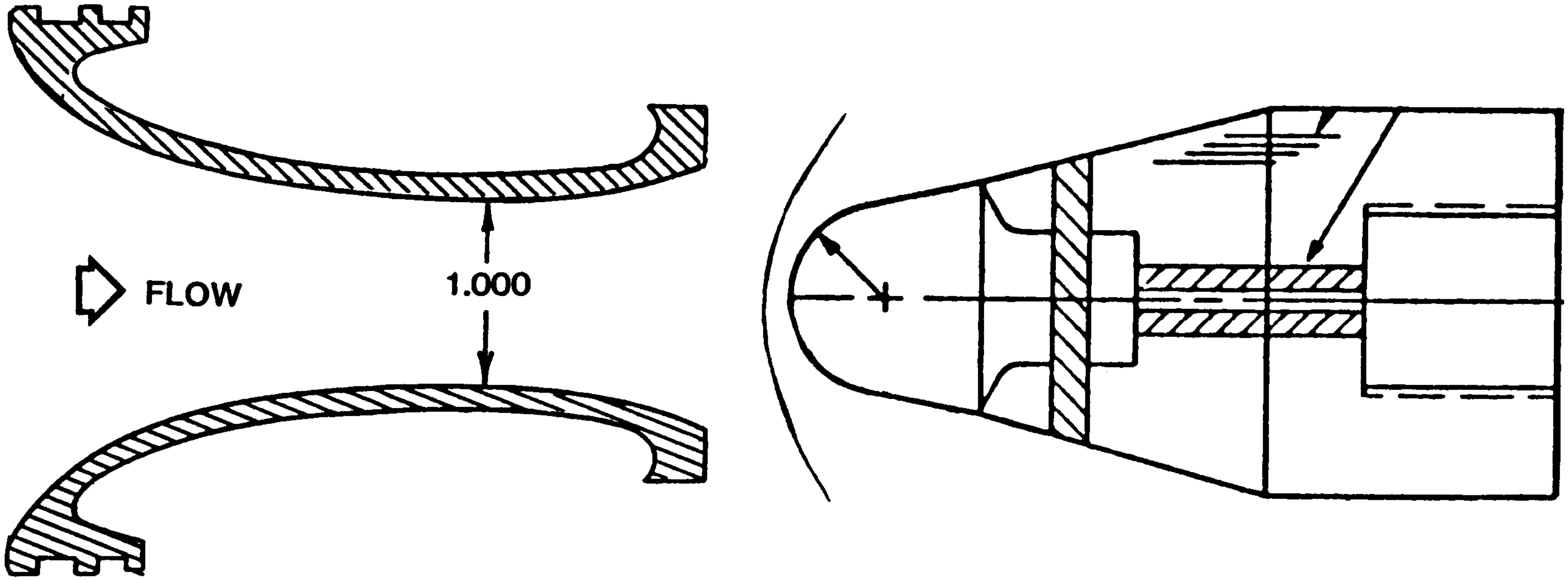

Figure 11. Transition Model and Flared Nozzle

exit. Although the total pressure in the flow stays constant, the total pressure behind the standoff shock (P_0') will decrease dramatically at stations farther downstream from the nozzle exit. Figure 12 shows the total pressure ratio (P_o'/P_{ch}) versus axial location from the nozzle exit. This flow expansion feature of the flared nozzle allows for transition testing to be accomplished in the arc tunnel.

Diagnostic probes are used to measure flowfield parameters in the expanding jet. The pitot-pressure probe and the heat-transfer probe are shown in Figure 13. The pressure probe contains a piezoelectric transducer and the heat transfer probe contains a null-point calorimeter slug. These probes are swept through the supersonic flowfield at the 2.5-inch and .1-inch axial stations to obtain radial profiles of the pitot pressure and the heat flux. Typical results of a pressure sweep at the 2.5-inch station are shown in Figure 14. Results from a calorimeter sweep are shown in Figure 15.

Now that we know the internal tunnel conditions and some flowfield parameters, we can calculate two important enthalpies. The bulk enthalpy is determined with an energy balance calculation which calculates the energy left in the flowfield after water cooling losses. The bulk enthalpy (H_B) is calculated using:

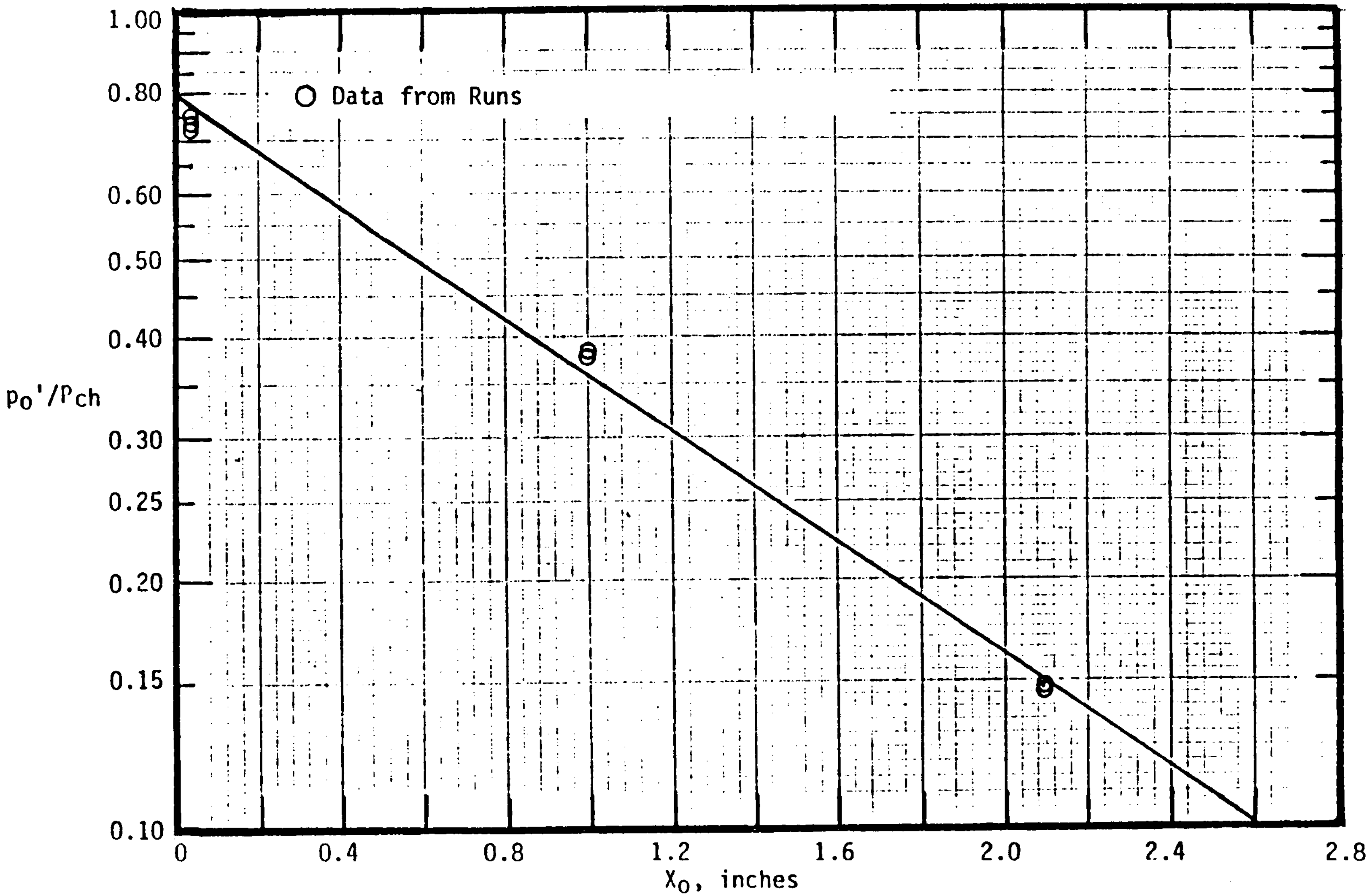

Figure 12. Pressure Ratio at Nozzle Stations

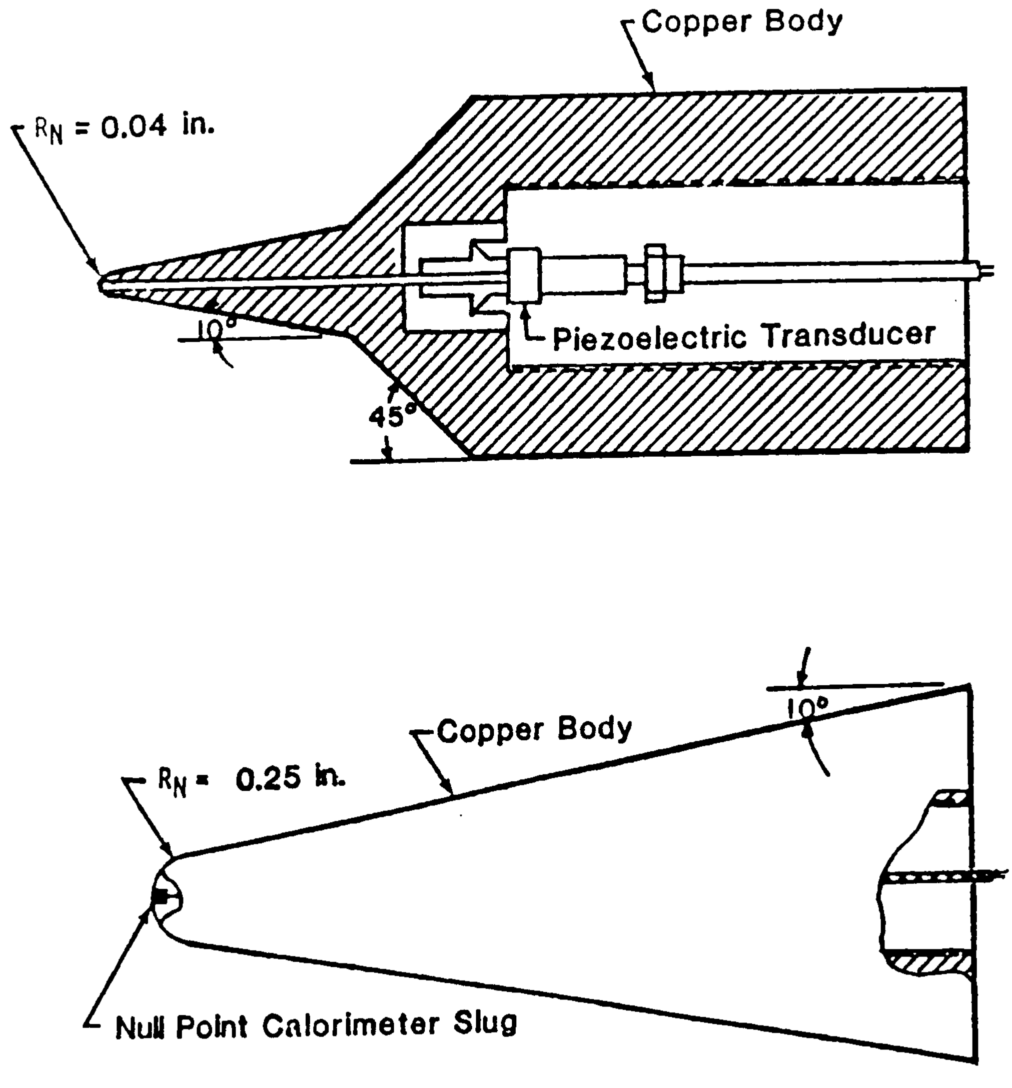

Figure 13. Pressure Probe and Heat Transfer Probe

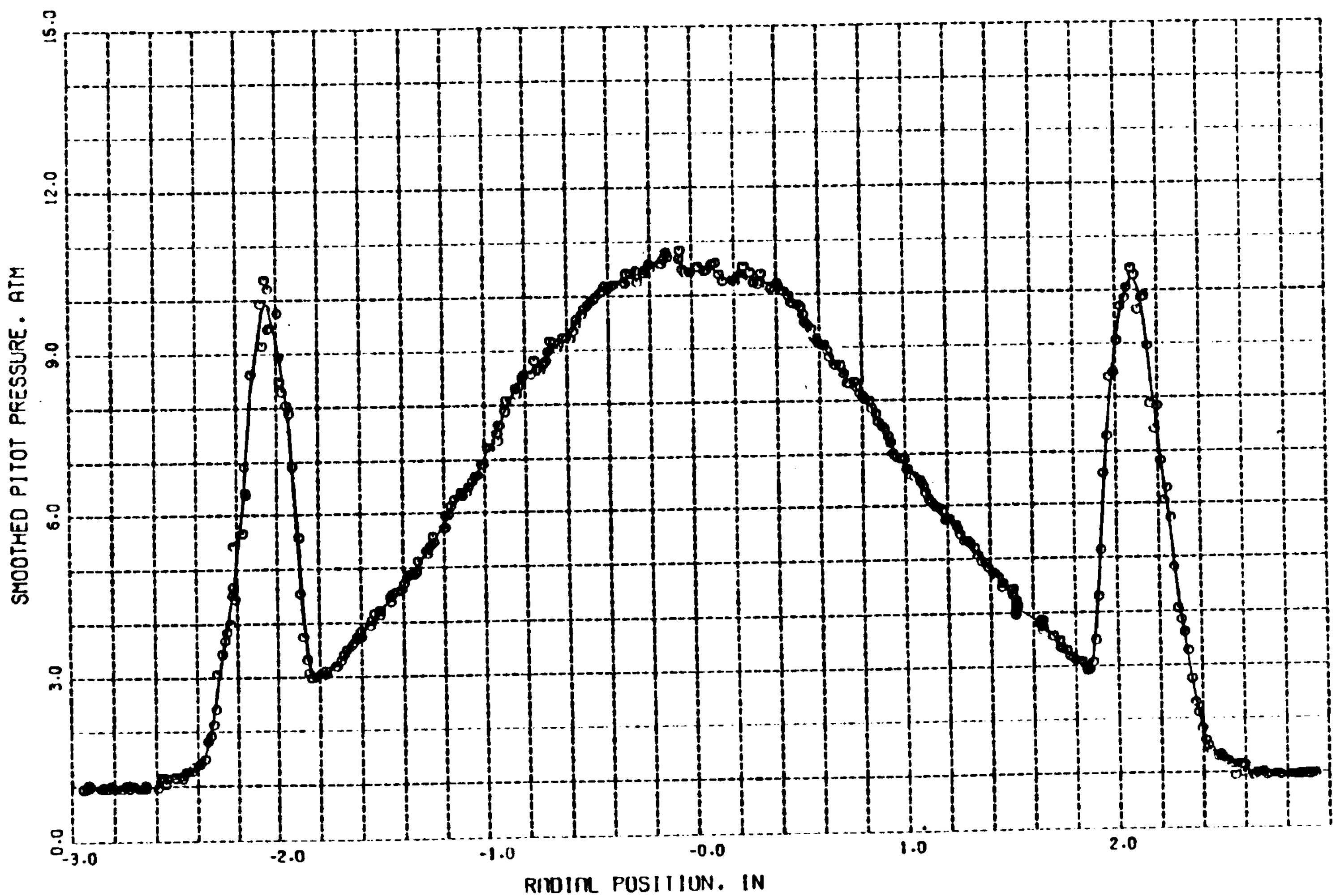

Figure 14. Pitot Pressure Across Nozzle at 2.5 Inch Station

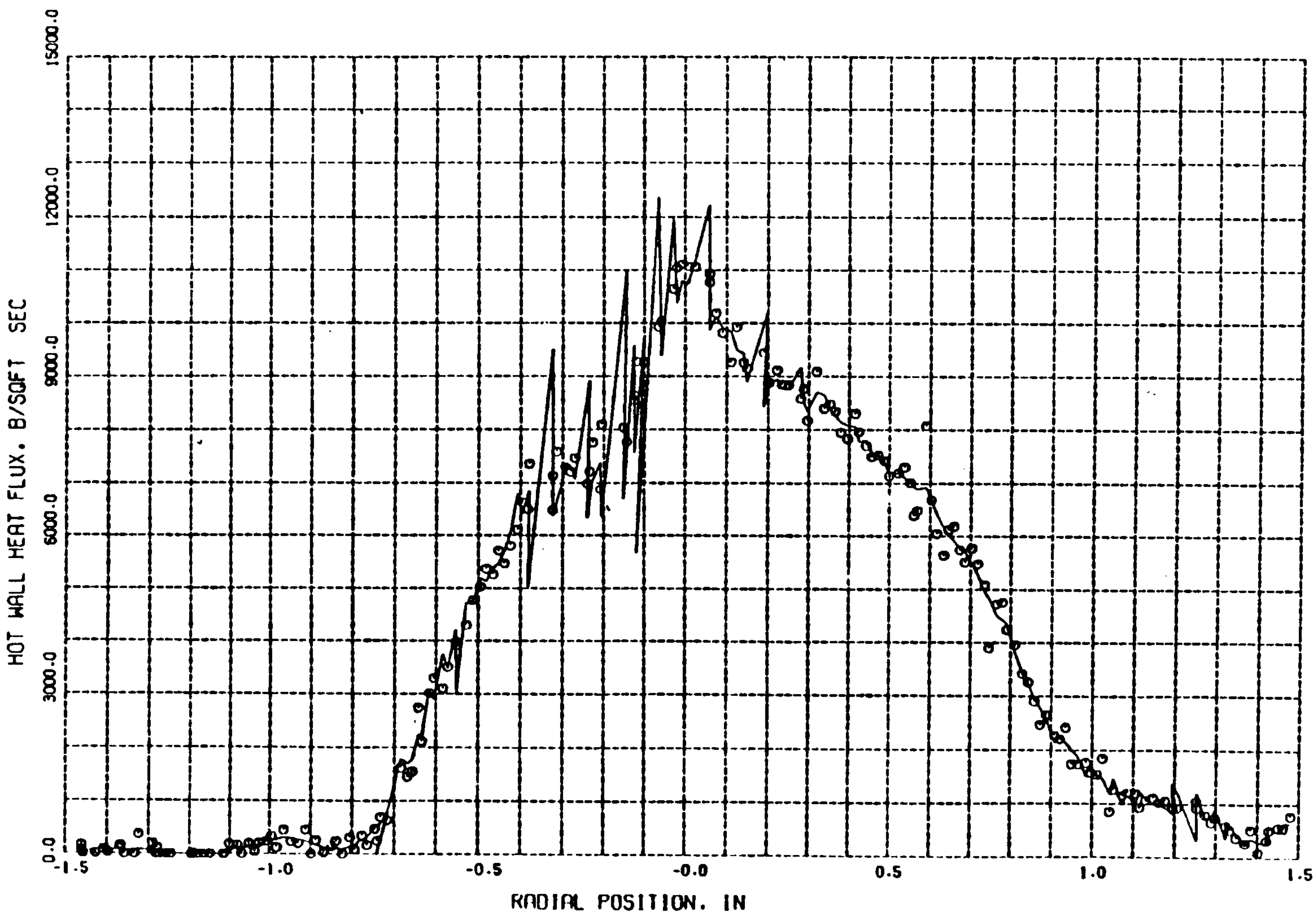

Figure 15. Heat Transfer Across Nozzle at .1 Inch Station

$$H_B = \left[k\,(PWR_{IN} - PWR_L)/\dot{M}_T \right] + H_I \qquad (44)$$

The bulk enthalpy is about 2500 Btu/lbm. From the measured heat flux and total pressure, the inferred enthalpy (H_{INF}) can be calculated using the Fay-Riddell equation for heat flux on the stagnation point of a hemisphere.

$$H_{INF} = \left[6.882\,\dot{Q}_o/(P_o^{'}/R_N)^{1/2} \right] + H_w \qquad (45)$$

The inferred enthalpy is generally twice as large as the bulk enthalpy in arc-heated wind tunnels. This paradox will cause a problem when trying to determine an enthalpy to use in further calculations. The arc-tunnel flowfield conditions are shown in Table 2.

Testing Technique

A model ramping technique is used to simulate reentry conditions on the model nosetip. The arc tunnel is started and is given time to reach steady state conditions. Once on condition, a computer-controlled model sequence is started and the model is injected into the flow at the 2.5-inch axial station for a 2.0 second-dwell. During the dwell, the model heats under low pressure conditions which simulates the high-altitude laminar heating on a RV. The models are then moved toward the nozzle exit at a rate of .6 in/sec for roughly four seconds. This ramp of

Table 2. Arc Tunnel Operating Conditions

Run Number	Probe	Axial Station, in	Pch*, atm	Po' atm	H_{OINF}, Btu/lbm		$\dot{q}_{OHW}$, Btu/ft^2 sec		Tw, °R	Nozzle
					Peak	Avg**	Peak	Avg**		
Heat Transfer	0.5-1-21	0.10	97.3	72.0	5325	4650	12,500	10,800	1050	Flared d*=1.00 in. d_E=1.38 in.
Pressure	BL-101	2.50	90.5	10.6	N/A	N/A	N/A	N/A	N/A	Flared d*=1.00 in. d_E=1.38 in.

increasing pressure simulates the RV decreasing in altitude and Mach number. The model boundary layer will undergo transition from laminar to turbulent during the pressure ramp. The arc tunnel produces true flight temperatures for realistic flight times; therefore, the model nosetip will reach carbon sublimation temperatures. The sublimating carbon adds blowing to the nosetip boundary layer. When the model reaches the .1-inch axial station, the model is laser controlled in order to measure steady state-ablation rates at that given station.

The primary data are 16-mm motion pictures which are taken during the testing sequence. Boundary-layer transition data is obtained by examining the film data during the ramp phase. The data of interest from the ramp phase are the nosetip shape change profiles at different times in the sequence. The shape change profiles from one model are plotted in Figure 16. Generally, traces of the projected nosetip images are made at approximately .6-second intervals, although a trace is also made when any significant nosetip shape change is observed. Boundary-layer transition is observed by the increased ablation rate at the outer edge of the model. The higher ablation rate is caused by the increased heating rate which results from the turbulent boundary layer. This is seen by the gouging of the model material in sequential nosetip traces. As the

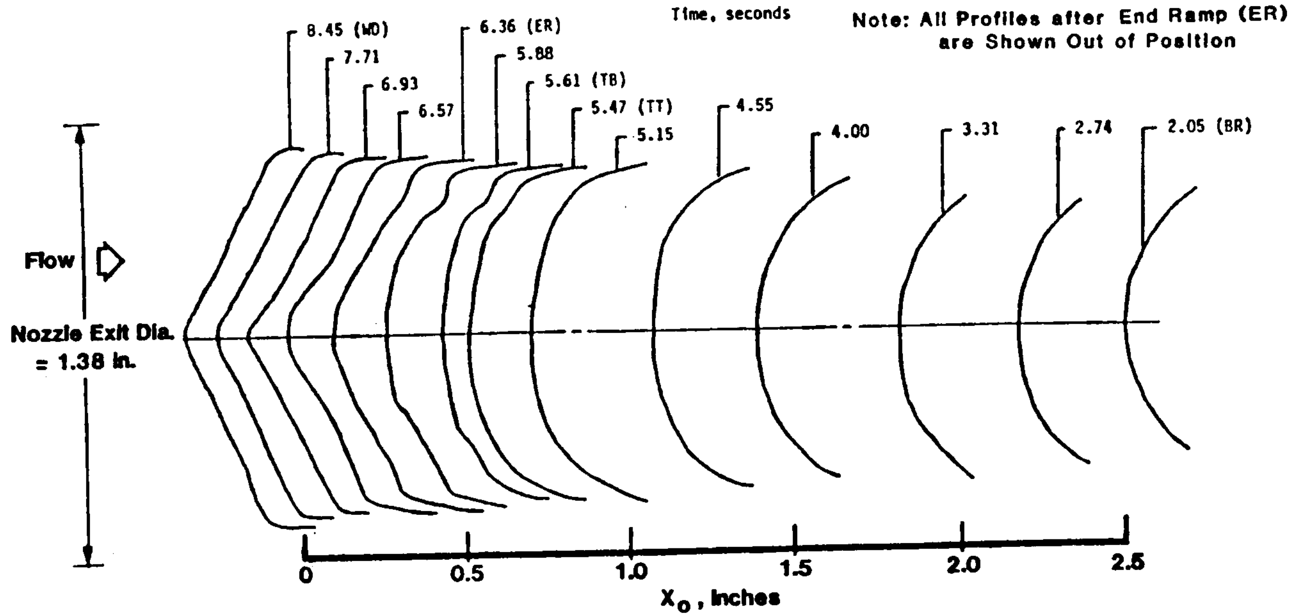

Figure 16. Nosetip Profile Shape Change

model progresses, the transition point will eventually move to the stagnation point and the model will form a pointed shape (fully turbulent shape). Once the model has reached a fully turbulent shape, turbulent recession rates can be measured and compared to the laminar recession rates (Figure 17). Typically, the turbulent recession rate is roughly twice the laminar ablation rate.

Data

Two models made of the same material were tested in the arc tunnel. Using this data, transition onset pressure and turbulent recession rates were determined and tabulated in Table 3. The transition-onset pressure was measured by interpreting the transition location and ramp time which are shown in Table 4. The transition location (streamlength) is measured from the stagnation point. Other interesting data is the progression of the transition location. Two later transition progression data points, for each model, were selected and tabulated to show how the transition point moves toward the stagnation point as the flowfield pressure increases. This data will be used to compare with past results and ballistic range data from the same material.

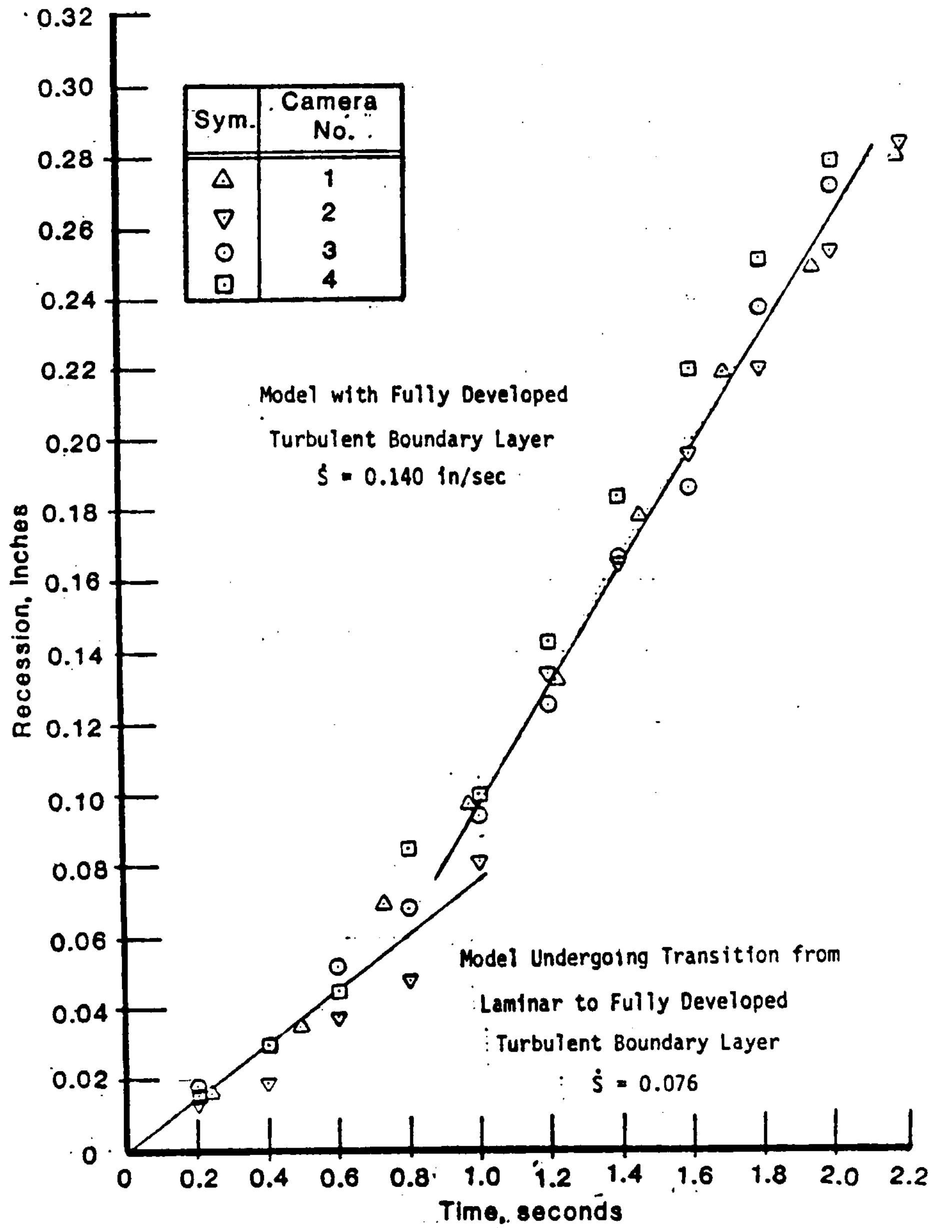

Figure 17. Nosetip Recession Graph

Table 3. Arc Model Recession Data

MODEL NUMBER	Transition Pressure (Atm)	RECESSION RATE (in/s)
1	57	.14
2	54	.16

Table 4. Arc Model Transition Data

Model	Type	Time (S)	Location (In)
1	Onset	5.89	.27
1	Progression	6.36	.15
1	Progression	6.36	.27
2	Onset	5.50	.35
2	Progression	6.21	.23
2	Progression	6.21	.21

CHAPTER V

BALLISTIC RANGE TESTING

The ballistic-range ground-test facility can subject models to a short duration, real gas hypersonic environment. To date, the most comprehensive study of nosetip boundary layer transition in the ballistic range was completed by Reda in [14]. The ballistic range can provide actual RV velocities with a variety of pressures to account for altitude changes. But the ballistic range can not duplicate actual RV flight times. For the purpose of nosetip boundary layer transition, the reduced testing time will affect the problem in two ways. First, the nosetip will not reach true RV wall temperatures. Secondly, the nosetip material will not have enough time to produce accurately the laminar surface roughness. The wall temperature difference can be included and adjusted for in all the current correlations. But the laminar heated surface roughness for a ballistic-range model nosetip must be provided to the material before launch.

Material Preconditioning

Because the flight time in a ballistic range is relatively short, boundary-layer transition models must be provided with their laminar heating surface roughness. This is accomplished by subjecting the nosetip material to the flow of an arc-heated wind tunnel. The process is identical to the beginning of an arc tunnel transition test described in Chapter IV. The nosetip material sample is mounted to a model holder (Figure 18). The model is injected into the low pressure region ($P_o' = 10\,Atm$) of the arcjet for a duration of two seconds which provides a laminar boundary layer around the nosetip. The low-pressure arcjet simulates the high-altitude heating encountered by a RV. The nosetip material will ablate about 40 mils. The nosetip samples are then unscrewed from the arc model holders and attached to the ballistic range model bases (Figure 19). At least one extra nosetip sample is preconditioned for further surface characterization.

The extra nosetip sample is cross-sectioned and microscopic photographs (microscopy) of its surface roughness are taken. Batt and Legner [1] standardized a method to calculate the material surface roughness (k). First, an arbitrary reference (y_0) is chosen. The surface is then divided into many equally spaced stations. At each point, the difference between the reference and the surface height ($y_s - y_o$) is calculated. These values are then arranged into different bins according to their magnitude. From these bins, a probability of exceedance curve can be constructed, top of Figure 20. As ($y_s - y_o$) gets smaller, fewer points will contribute to the probability of

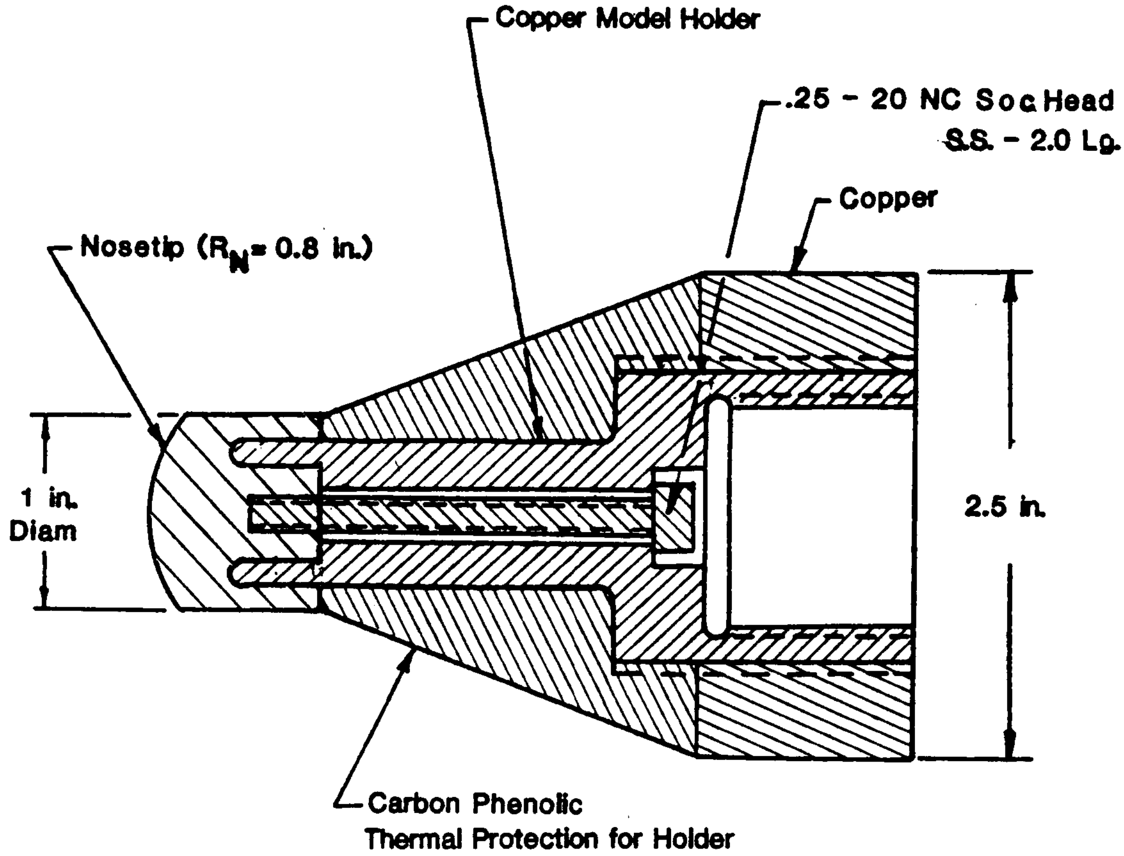

Figure 18. Material Preconditioning Model

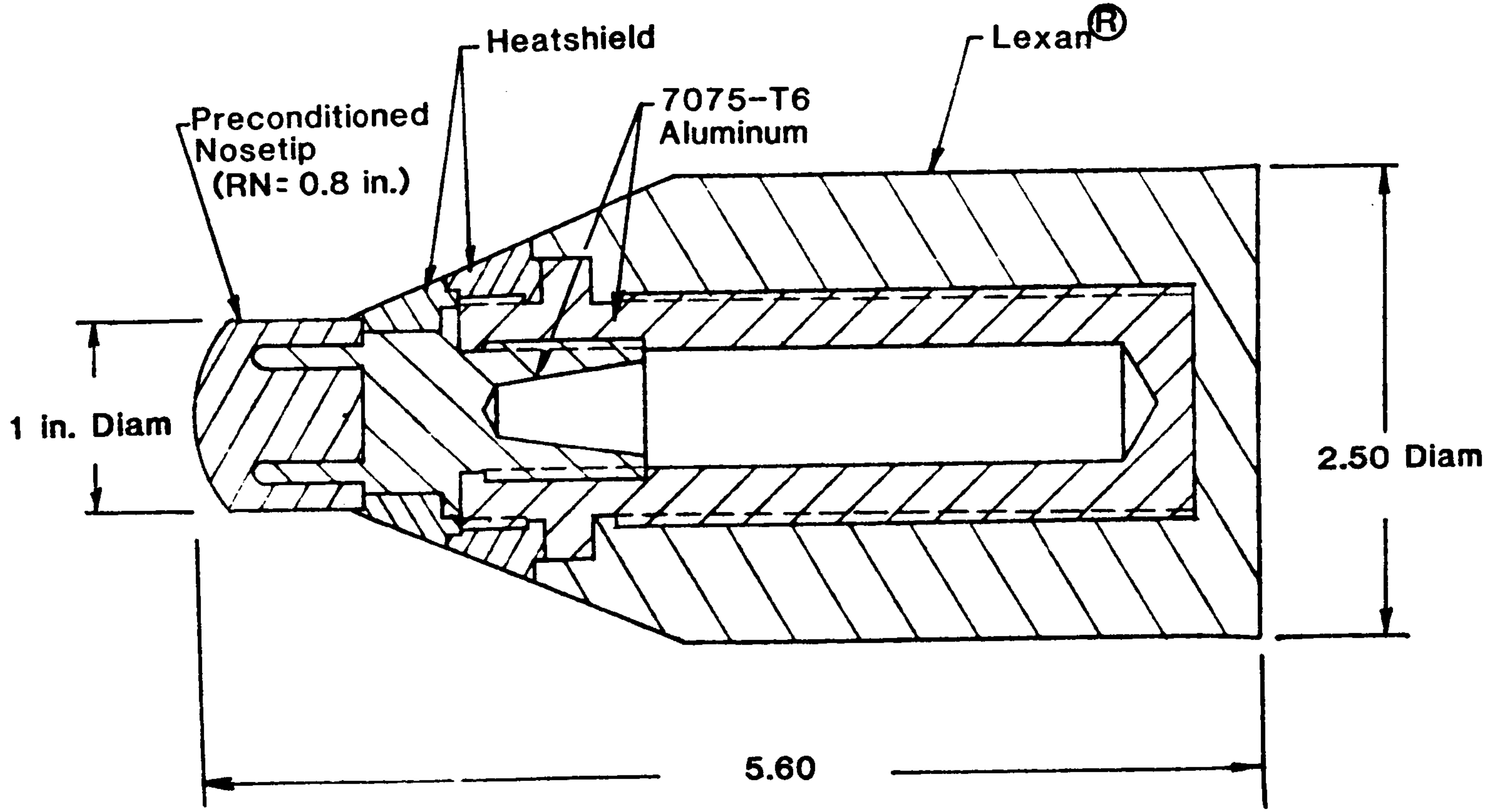

Figure 19. Ballistic Range Model

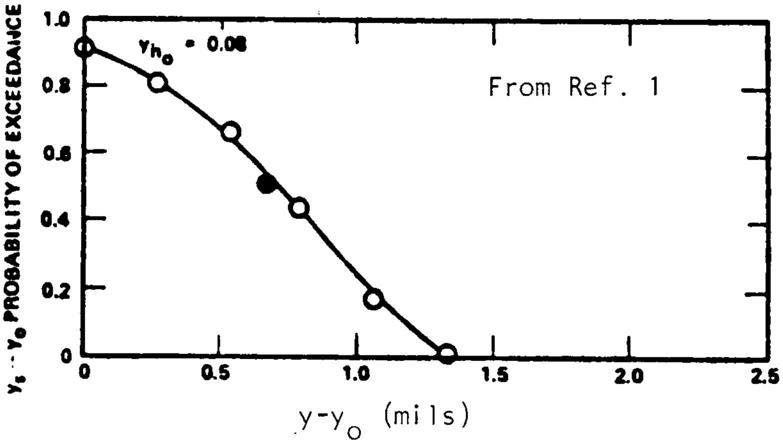

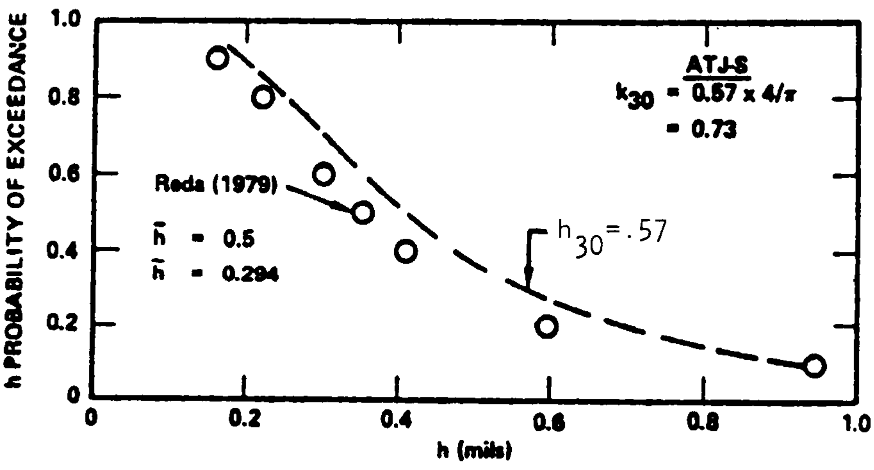

Figure 20. Probability of Exceedance Curves

exceedance curve and the data will roll over. A new baseline reference (y_{ho}) is determined by fitting the data between a probability of 20 and 80 percent using a straight line and determining the roughness height where the probability is equal to 100 percent. The baseline reference will be a positive number; in this graph, it was measured to be .08 mils. A new probability of exceedance curve is now determined using the new baseline reference. This is called the roughness height probability of exceedance and is shown at the bottom of Figure 20. The curve typically has a Gaussian profile from which one can choose the 30 percent exceedance value (h_{30}). Finally, this number is adjusted by the shape factor (F), where:

$$k_{30} = F h_{30} \tag{46}$$

Dirling defined the shape factor to account for the fact that any plane of measurement does not pass through the peak of each roughness element. Therefore, the measured roughness (h_{30}) is too low. The most popular shape factor is the hemispherical ($4/\pi$), but 2 has sometimes been used for carbon-carbon composite materials. Because there is a lack of carbon-carbon data, we will analyze the data using the more common hemispherical shape factor.

Testing Technique

After the surface roughness is characterized, the models are launched from a two-stage light-gas gun into a controlled atmospheric range. For the tests considered here, the range pressure was 175 torr, which simulates an altitude of 36,000 feet. The launch velocity was 16,000 ft/sec. At this velocity and pressure, the transition location will be upstream of the sonic line on the nosetip surface. Image converter cameras are used to take photographs of the model as it travels downrange. The image converter negatives are processed with an isodensitometer which defines the relative film density as a function of surface location. Each film density is equivalent to a surface temperature on the nosetip of the model. From this data, a surface temperature map of the nosetip is constructed (Figure 21). In Figure 21, the nosetip is travelling toward the camera (five degrees of yaw) and the cool laminar island can be seen around the stagnation point on the nosetip. Actual surface temperatures can be determined and graphed versus film location (Figure 22). In this graph, the higher temperature transition region can easily be seen on each side of the nosetip. The transition streamlength (S_{TR}) is the distance measured from the stagnation point to the positive change in slope of the temperature curve. The model nosetip

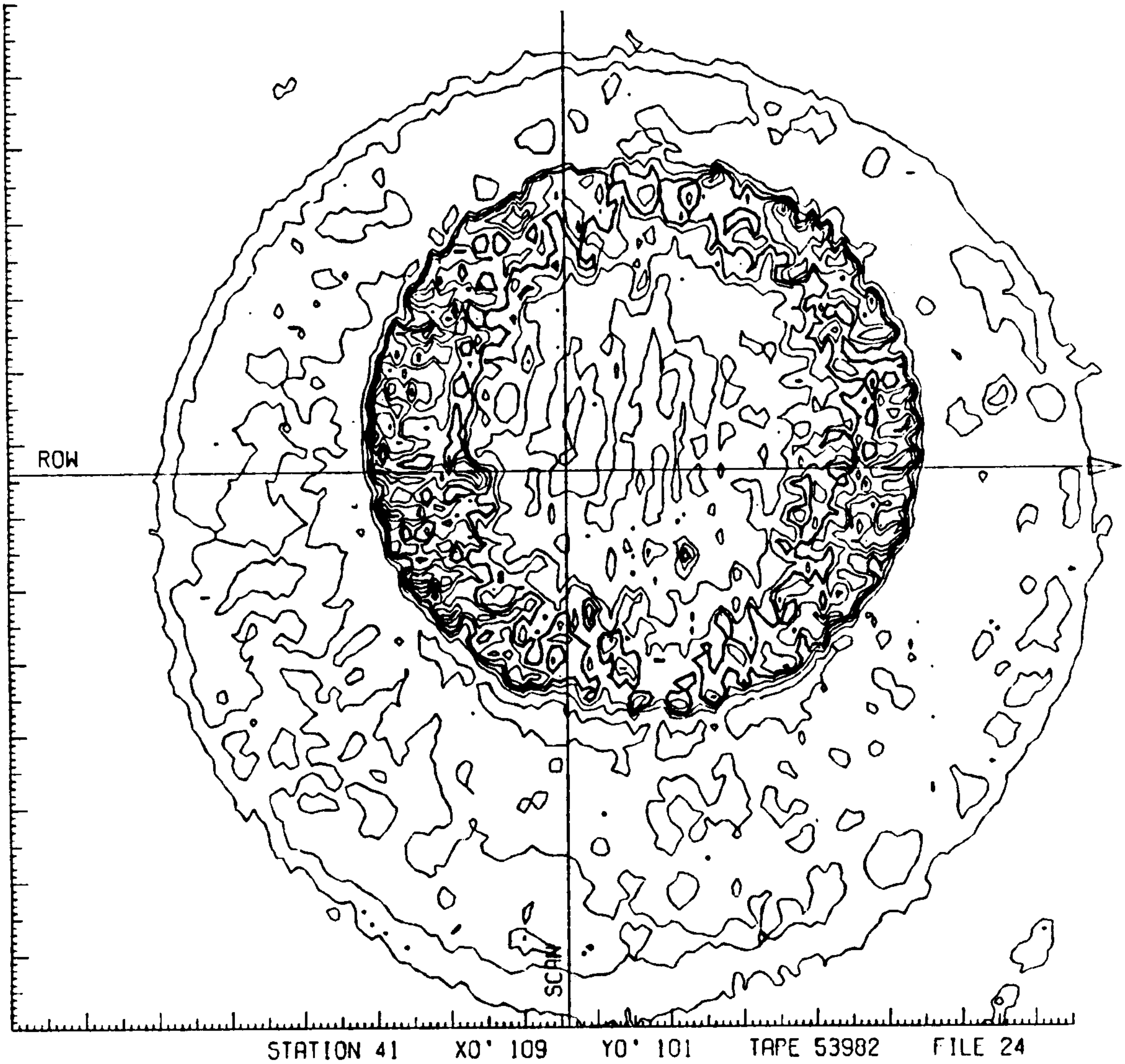

Figure 21. Nosetip Surface Temperature Map

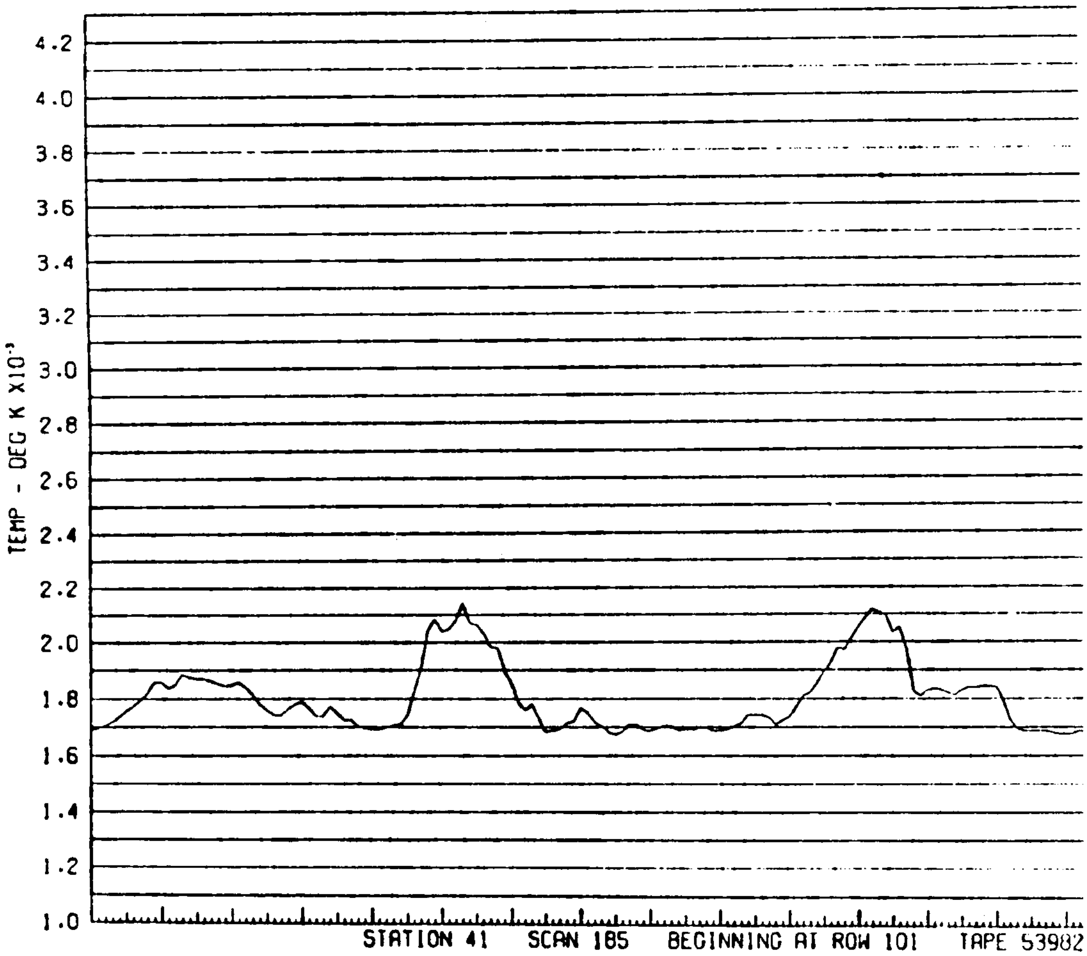

Figure 22. Nosetip Surface Temperature Graph

material will not reach sublimation temperatures of carbon, but the carbon material will oxidize producing a small amount of ablation (blowing into the boundary layer).

Data

Transition data can be taken at many different stations in the ballistic range. The transition location will change as the model travels downrange because the model decelerates and the nosetip surface temperature increases. This characteristic of a ballistic range test produces more than one data point per shot and helps us understand the transition location progression (slope of the correlation line). Two shots were performed using the same nosetip material as the arc tunnel data. The transition locations are tabulated at different range stations in Table 5; this data will be analyzed in Chapter VI.

Table 5. Ballistic Range Transition Data

Model	Time (S)	S_{TR} (in)
1	.005	.29
1	.015	.23
1	.025	.29
1	.04	.33
1	.05	.23
2	.025	.27
2	.04	.26

CHAPTER VI

DATA ANALYSIS

This chapter contains analysis of the arc-tunnel and ballistic-range data presented in the earlier chapters. Using the Batt and Legner Correlation and a boundary-layer computational code, an inferred material roughness (k_{INF}) was calculated for each data point. The actual material roughness (k_{30}) was then determined from the microscopy photographs of the preconditioned nosetips. Therefore, knowing the actual material roughness, the ground test data can be directly compared to the Batt and Legner correlation. And finally, a new correlation is suggested to help correct for the differences in the test data.

Arc Inferred Roughness

Using the boundary-layer transition data obtained in the arc tunnel, and assuming it fits the Batt and Legner correlation, an inferred material roughness height (k_{INF}) can be determined by solving for k in:

$$R_{e\theta} = 500 \left[\frac{k}{\Theta} \frac{T_e}{T_w} \frac{}{(1 + 350 \frac{k}{R_n})} \right]^{-1.5} \qquad (47)$$

The transition location is known from the film data. Therefore, the boundary layer conditions can be calculated at the transition streamlength. The ABRES Shape Change

Code (ASCC 86) [9] was utilized to determine the edge temperature (T_E), wall temperature (T_w), momentum thickness (Θ), and the momentum thickness Reynold's number ($R_{e\Theta}$). ASCC was written by Acurex to model RV nosetip shape change during flight, ballistic-range, arc-tunnel, and wind tunnel testing. The arc tunnel option was used and the arc conditions were programmed in the ASCC code. The code solves a viscous, compressible integral-boundary-layer equation which assumes a smooth wall, no blowing, and chemical equilibrium. Thus, the values determined by the code are used as reference quantities for comparison between correlations. An example of an ASCC boundary layer solution is shown in Table 6. The nosetip radius was measured from the film data at the time of transition. As mentioned earlier, the flowfield enthalpy of the arc tunnel is difficult to determine. For this test, the bulk enthalpy was 2500 Btu/lbm, while the centerline inferred enthalpy was 5200 Btu/lbm. Because this disparity exists, two inferred material roughnesses were calculated for comparison. The arc tunnel transition location, ASCC-calculated boundary-layer conditions, and the resulting bulk-enthalpy inferred roughnesses are tabulated in Table 7. A similar calculation was used to determine the inferred roughness produced when using the peak (centerline inferred) enthalpy (Table 8).

Table 6. ASCC Boundary Layer Solution

ABRES SHAPE CHANGE CODE (ASCC)

TIME = 6.000000

VISCOUS FLOW - BOUNDARY LAYER SOLUTION

BODY PT NO (J)	INTEG PT NO (I)	STREAM LENGTH INCH (S)	MOMENTUM THICKNESS MIL (THE)	ENERGY THICKNESS MIL (PHI)	SHAPE FACTOR (HSF)	MOM-THICK RE NO (RETH)	ENERGY-THICK RE NO (REPH)	HEAT TRANS COEFFICIENT LBM/FT2-SEC (RUCH)	REYNOLDS ANAL FAC (RAF)	INTER-MITTENCY (ADML)
1	1	0.0000	0.215	0.400	2.046	0.000E+00	0.000E+00	8.817E-01	0.6966	0.00
2	7	0.0515	0.217	0.400	2.047	1.676E+01	3.089E+01	8.809E-01	0.6988	0.00
3	9	0.1031	0.211	0.403	2.049	3.229E+01	6.164E+01	8.768E-01	0.6728	0.00
4	11	0.1547	0.208	0.407	2.052	4.701E+01	9.198E+01	8.695E-01	0.6569	0.00
5	13	0.2062	0.210	0.412	2.057	6.217E+01	1.219E+02	8.604E-01	0.6574	0.00
6	15	0.2578	0.213	0.418	2.063	7.705E+01	1.512E+02	8.484E-01	0.6594	0.00
7	17	0.3094	0.217	0.426	2.070	9.154E+01	1.797E+02	8.341E-01	0.6616	0.00
8	19	0.3610	0.222	0.436	2.079	1.055E+02	2.072E+02	8.177E-01	0.6642	0.00
9	21	0.4126	0.228	0.448	2.089	1.190E+02	2.339E+02	7.992E-01	0.6664	0.00
10	23	0.4642	0.235	0.461	2.100	1.321E+02	2.595E+02	7.794E-01	0.6690	0.00
11	25	0.5159	0.243	0.476	2.114	1.449E+02	2.843E+02	7.584E-01	0.6726	0.00
12	27	0.5675	0.252	0.493	2.128	1.572E+02	3.073E+02	7.331E-01	0.6798	0.00
13	29	0.6192	0.264	0.513	2.142	1.688E+02	3.283E+02	7.058E-01	0.6889	0.00
14	31	0.6709	0.271	0.543	2.159	1.764E+02	3.539E+02	6.883E-01	0.6533	0.00
15	33	0.7227	0.288	0.560	2.176	1.876E+02	3.655E+02	6.504E-01	0.6940	0.00
16	35	0.7745	0.307	0.591	2.189	1.985E+02	3.822E+02	6.138E-01	0.7094	0.00
17	37	0.8263	0.326	0.626	2.209	2.084E+02	3.998E+02	5.823E-01	0.7126	0.00
18	39	0.8781	0.348	0.663	2.226	2.179E+02	4.150E+02	5.483E-01	0.7227	0.00
19	41	0.9299	0.372	0.705	2.244	2.264E+02	4.291E+02	5.161E-01	0.7284	0.00
20	43	0.9818	0.397	0.752	2.262	2.337E+02	4.420E+02	4.856E-01	0.7283	0.00
21	45	1.0338	0.425	0.811	2.284	2.385E+02	4.551E+02	4.584E-01	0.7104	0.00
22	47	1.0857	0.457	0.873	2.307	2.430E+02	4.644E+02	4.267E-01	0.7064	0.00
23	49	1.1377	0.495	0.935	2.325	2.483E+02	4.696E+02	3.953E-01	0.7145	0.00
24	51	1.1897	0.540	1.001	2.338	2.552E+02	4.734E+02	3.637E-01	0.7329	0.00
25	53	1.2417	0.589	1.044	2.324	2.665E+02	4.725E+02	3.301E-01	0.8001	0.00
26	55	1.2938	0.632	1.046	2.277	2.815E+02	4.659E+02	2.944E-01	0.9376	0.00
27	59	1.5009	0.757	1.106	2.198	3.354E+02	4.900E+02	2.512E-01	1.1393	0.00

Table 7. Inferred Roughness, Arc Bulk Enthalpy

Model	Time (Sec)	S_{TR} (in)	T_E(R°)	T_W(R°)	Θ (mil)	$R_{e\Theta T}$	K_{INF}
1	5.89	.27	7,230	6,385	.218	82	.86
1	6.36	.15	7,340	6,485	.196	50	1.16
1	6.36	.27	7,270	6,450	.202	86	.75
2	5.50	.35	7,130	6,270	.244	94	.88
2	6.21	.23	7,290	6,452	.202	72	.87
2	6.21	.21	7,300	6,458	.201	67	.92

Table 8. Inferred Roughness, Arc Peak Enthalpy

Model	Time (Sec)	S_{TR} (in)	T_E(R°)	T_W(R°)	Θ (mil)	$Re_{\Theta T}$	K_{INF}
1	5.89	.27	11,210	7,328	.319	62	1.25
1	6.36	.15	11,405	7,417	.287	37	1.80
1	6.36	.27	11,300	7,390	.294	67	1.03
2	5.50	.35	11,060	7,223	.353	72	1.24
2	6.21	.23	11,325	7,388	.296	54	1.28
2	6.21	.21	11,345	7,390	.295	51	1.33

The bulk-enthalpy inferred roughnesses are low when compared to the actual material roughness. The bulk enthalpy inferred roughnesses are all around .9 mils, but the roughnesses determined from the peak enthalpy (roughly 1.20 mils) seem to be in close agreement with the actual material roughness (1.15 mils). Physically this seems reasonable, because the boundary layer is most affected by the centerline flowfield expanding from the stagnation point; therefore, it is more representative of the centerline peak inferred enthalpy. Later in this chapter, other correlations also show the peak enthalpy to yield the most consistent results.

Range Inferred Roughness

A similar method was used to analyze the ballistic range data. The transition location is read from the image converter photographic data produced at different range stations on two different shots. Once again, the ASCC code was utilized to determine the flowfield and boundary-layer conditions around the nosetip of the model. By assuming the Batt and Legner correlation is correct, an inferred surface roughness can be calculated to compare with the arc data. The ballistic range transition location, ASCC-calculated boundary-layer conditions, and the resulting inferred material roughnesses are tabulated in Table 9.

Table 9. Inferred Roughness from Range Data

Model	Time (Sec)	S_{TR} (in)	$T_E(R°)$	$T_W(R°)$	Θ (mil)	$Re_{\Theta T}$	K_{INF}
1	.005	.29	11,110	1,310	.356	104	.13
1	.015	.23	10,830	1,830	.343	79	.21
1	.025	.29	10,430	2,090	.344	96	.22
1	.04	.33	9,890	2,440	.339	109	.25
1	.05	.23	9,700	2,200	.327	77	.28
2	.025	.27	10,450	2,085	.342	92	.23
2	.04	.26	9,980	2,220	.334	85	.26

Note that all the range-inferred roughnesses are significantly low (around .25 mils). This is surprising, since it would be expected for the range data to more closely match the actual material roughness of 1.15 mils. It should be pointed out that the transition location does not seem to change significantly with range station. But, the wall temperature changes drastically from the beginning to the end of the range. Most of the available correlations would lead us to believe that this large change in wall temperature should effect the transition location more significantly than our range data indicates. The wall temperature never approaches true RV nosetip temperatures in the ballistic range. Therefore, the carbon does not sublimate and contribute a large blowing parameter to the boundary layer (although the carbon will oxidize and produce a small blowing effect).

Material Roughness

The carbon-carbon material which was tested in the ballistic range was preconditioned in the arc tunnel under the laminar heating method described in Chapter V. One of the nosetip samples was saved to be sectioned and microscopied. From the sectioned sample, microscopic photographs were taken of the material surface. The material surface was then graphed at 360 power, as shown in Figure 23. Station numbers are assigned to the x axis of

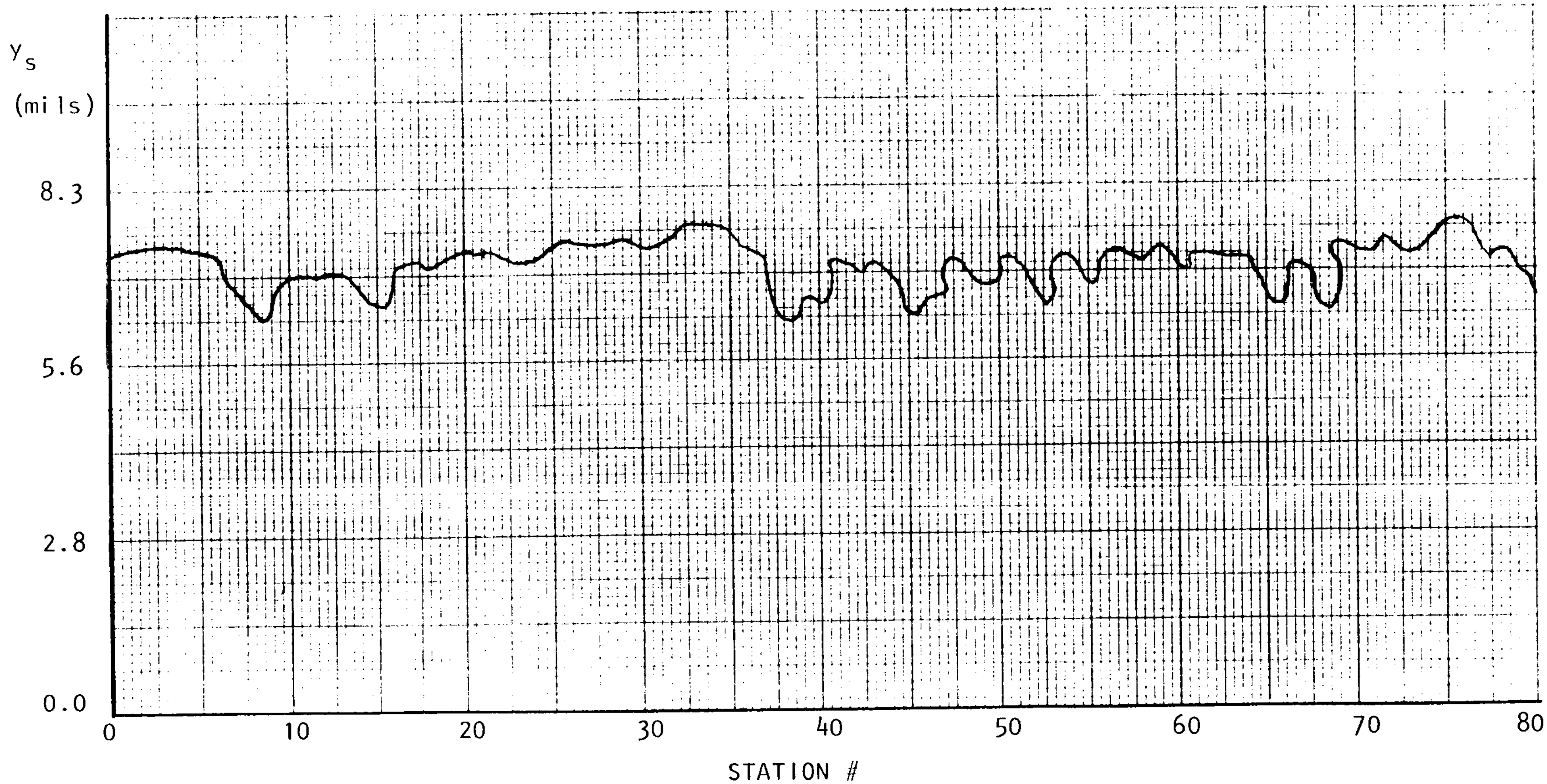

Figure 23. Material Surface Roughness

this graph to keep an accounting record of each roughness height versus station number. Using the Batt and Legner method, a reference height (y_o) is selected and the value of (y_s-y_o) is measured at each station. By grouping these values into bins, a material probability of exceedance curve is determined as shown in Figure 24. Fitting the data with a line between the 20 and 80 percent exceedance values determines the new material reference height (y_{ho}). Then a new probability of exceedance curve can be determined using the new reference height. The resulting curve is called the height probability of exceedance (Figure 25). To date, Batt and Legner reduced all the previous data sets by selecting the 30 percent exceedance value. The measured 30 percent exceedance height (h_{30}) for our material is .9 mils. As mentioned earlier and explained by Dirling, this value would be considered too low, because any plane of measurement would not pass through the peaks of each roughness element. Therefore, the roughness height is multiplied by a hemispherical shape factor ($4/\pi$) to determine the final material roughness value (k_{30}). The material roughness of our carbon-carbon material is then 1.15 mils.

Batt and Legner Correlation Fit

Characterization of the material roughness allows the arc and range data sets to be compared directly to the Batt

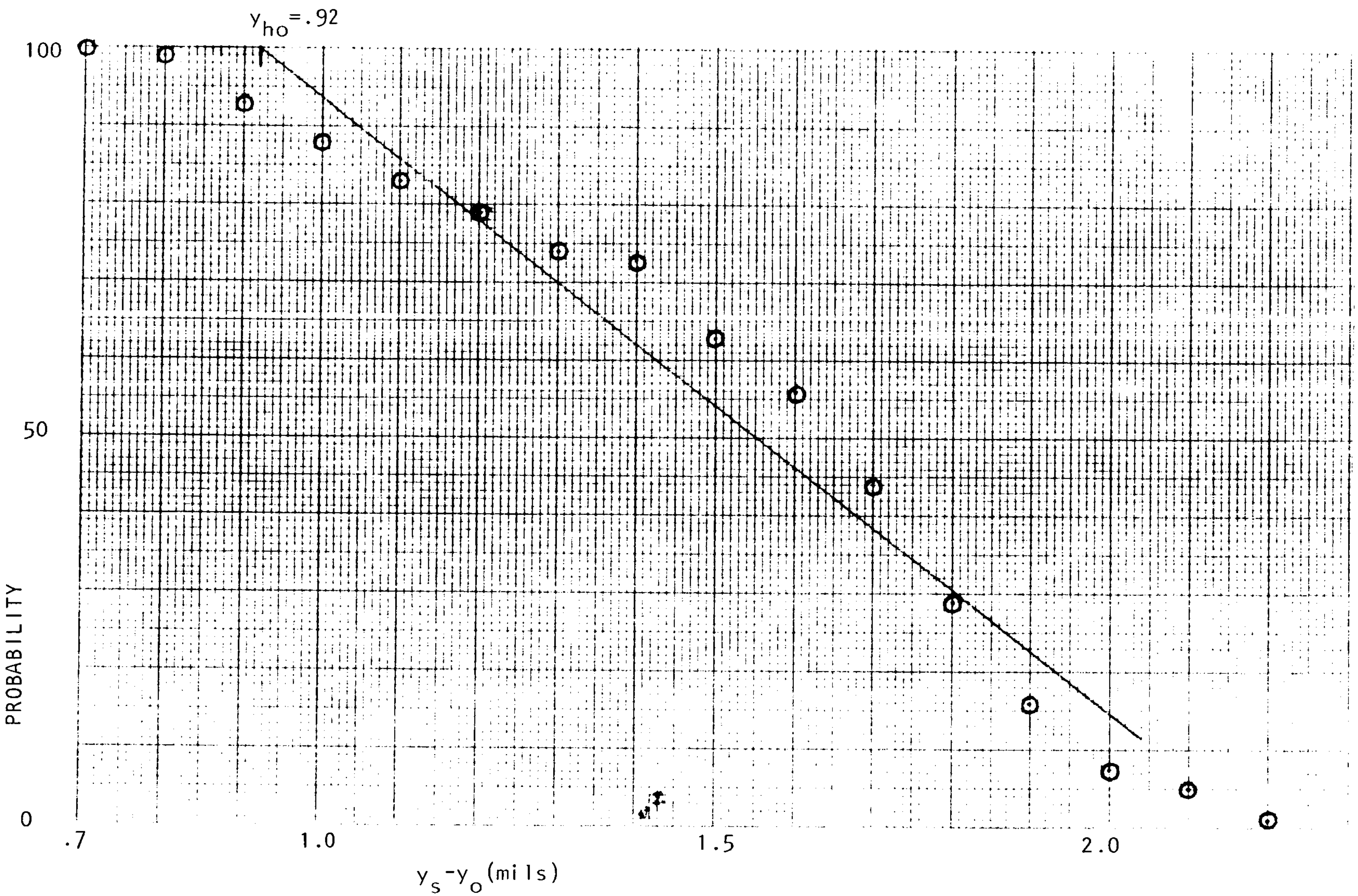

Figure 24. Material Probability of Exceedance

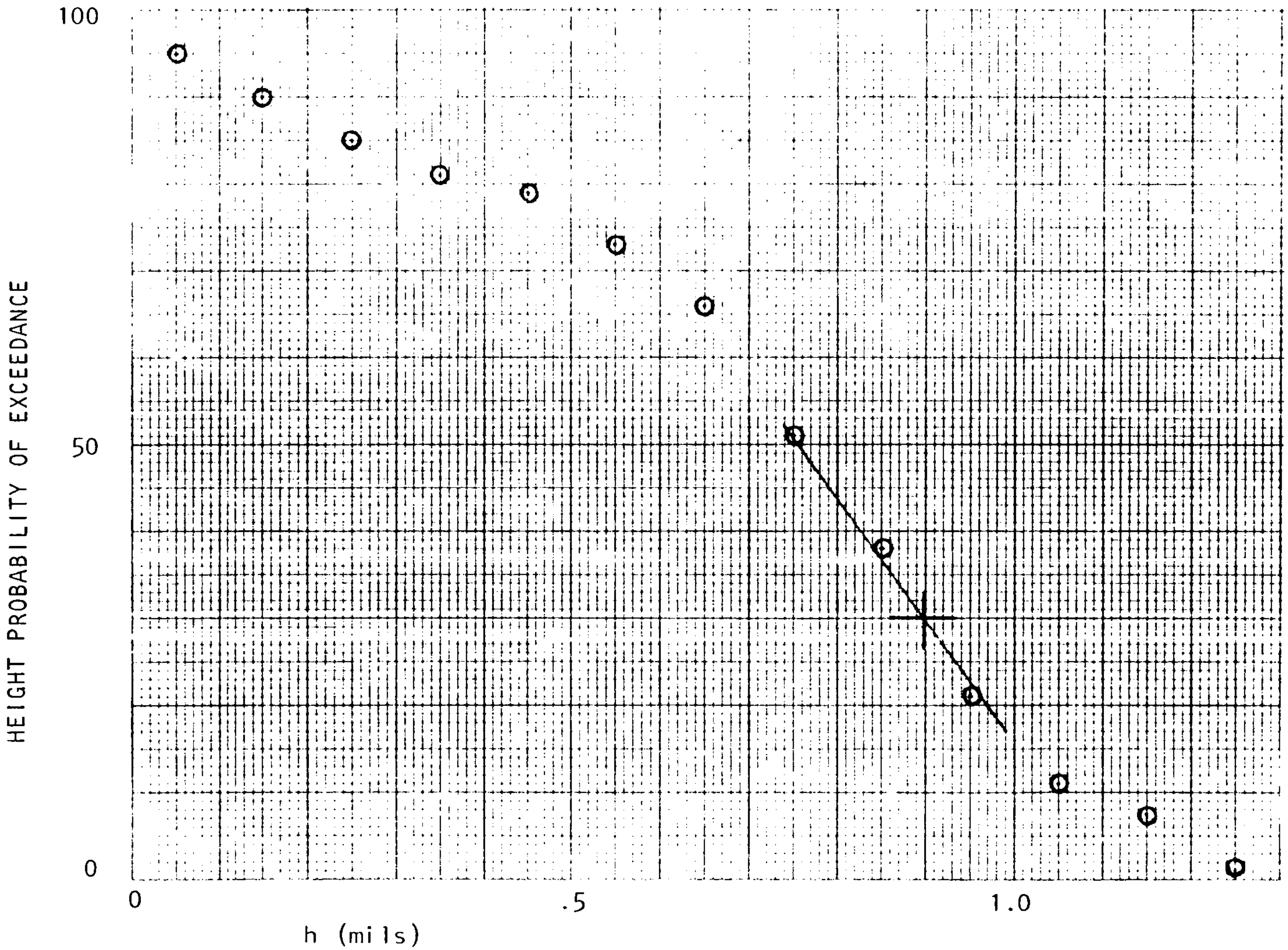

Figure 25. Height Probability of Exceedance

and Legner Correlation. The expected momentum thickness Reynolds number at transition can be calculated by using 1.15 mils for the material roughness height (k) and inserting the other known quantities into:

$$R_{e\theta} = 500 \left[\frac{k}{\Theta} \frac{T_e}{T_w} \frac{}{(1 + 350 \frac{k}{R_n})} \right]^{-1.5} \quad (48)$$

This prediction can be compared to the experimental transition-momentum-thickness Reynolds number for both the range and arc data sets. In Table 10, the expected and experimental momentum-thickness Reynolds numbers are tabulated. The percent difference is also calculated for these values. The arc and range data is graphed in Figure 26. The arc data is shown by squares and the range data by circles.

From the earlier calculation of the inferred material roughness, it is not surprising that the arc and range data do not match very well. However, it is significant that the arc data falls on the Batt and Legner curve within a reasonable band of error. This is the first time that experimental arc data (onset and progression) has accurately fit the predicted solution. But the range data requires some explanation. The ratio (T_e/T_w) seems to be driving the ballistic range data too strongly. It should be noted, if the wall temperature is slowly increased to

Table 10. Data Fit to Batt and Legner Correlation

	$\frac{KT_e}{\theta T_w \, (1 + 350\,K/R_n)}$	Batt and Legner $R_{e\theta T}$	Experimental $R_{e\theta T}$	% Error
RANGE	19.5	5.8	104	+ 1700
	14.1	9.4	79	+ 740
	11.9	12.2	96	+ 690
	9.8	16.3	109	+ 570
	11.1	13.6	77	+ 470
	12.0	12.0	92	+ 670
	11.0	13.6	85	+ 625
ARC	3.8	67	62	-7
	4.3	57	37	-35
	4.1	60	67	+ 12
	3.4	78	72	-8
	4.1	60	54	-10
	4.1	59	51	-14

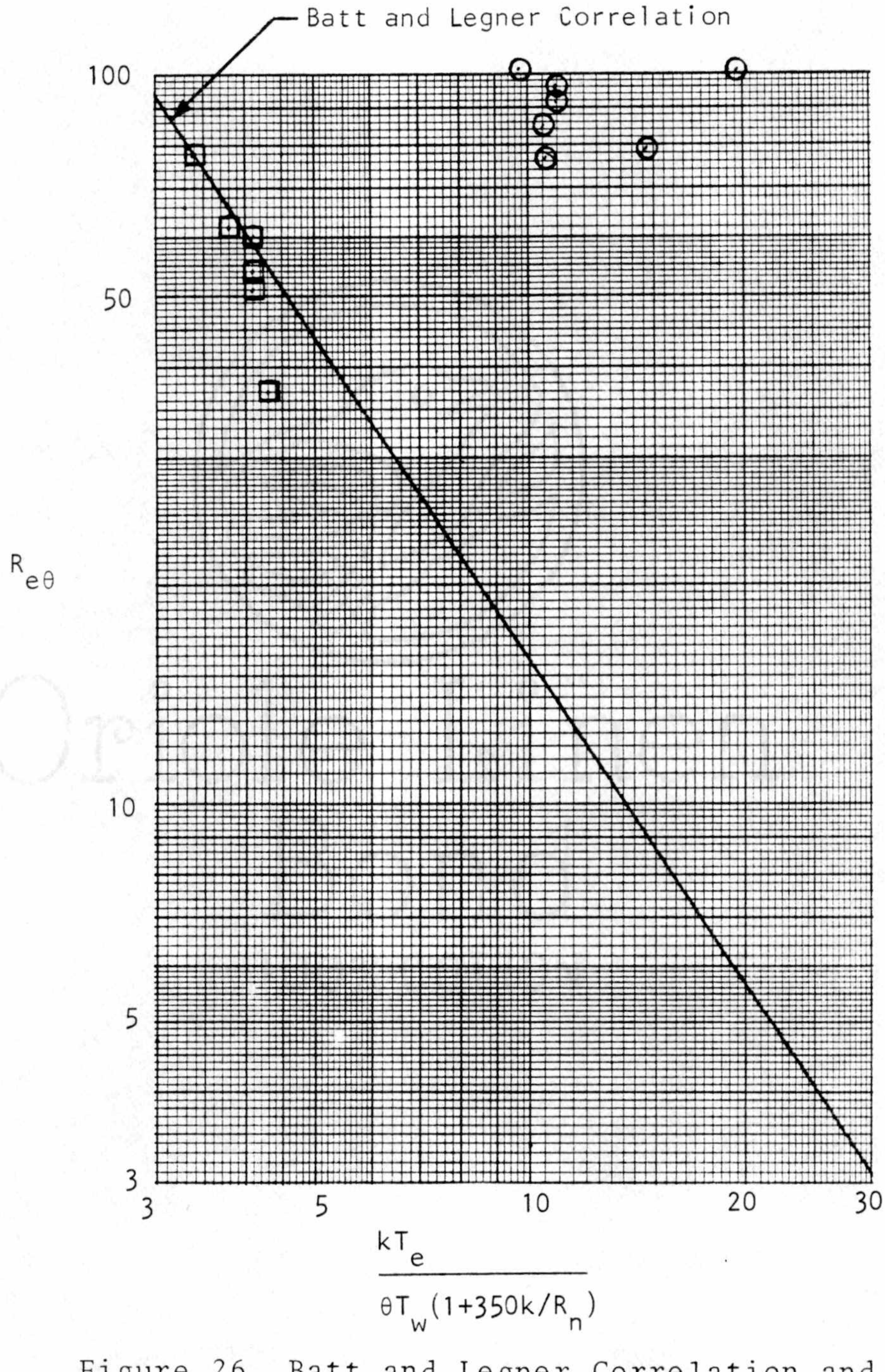

Figure 26. Batt and Legner Correlation and Plotted Data

roughly 70 to 80 percent of the edge temperature, the range data will move to the left on the graph and overlay the arc data. Thus, this would suggest a more simplified correlation excluding the temperature ratio may be interesting to investigate. In addition, the differences between the arc and range data may be explained by the significant destabilizing blowing produced by the sublimating carbon in the arc tunnel.

Revised Correlation

As suggested from the ballistic range data and the theoretical investigation in Chapter III, a correlation just including the material surface roughness, momentum thickness, and the momentum thickness Reynolds number should be investigated. The theoretical section suggested the following equation:

$$R_{e\theta} = C_1 \left(\frac{k}{\theta}\right)^{-C_2} \tag{49}$$

By taking the arc and range data, and curve fitting the equation to solve for the two unknown constants, one obtains:

$$R_{e\theta} = 18{,}500 \left(\frac{k}{\Theta}\right)^{-4.33} \tag{50}$$

This correlation produces remarkable agreement between the arc and range data. The experimental momentum thickness

Reynolds number, material roughness/momentum thickness ratio, inferred roughness, and the associated errors are tabulated in Table 11. The new correlation is plotted in Figure 27. The range data are again shown by circles and the arc data are represented by squares. The inferred material roughnesses are very near the actual value of 1.15 mils, with the largest deviation of 10 percent. For the limited data analyzed, the simplified correlation tends to confirm the relaxed effect of the wall temperature on the transition location.

Table 11. Data Fit to New Correlation

	$Re_{\theta T}$	$\frac{K}{\theta}$	K_{INF}	% Error
RANGE	104	3.23	1.17	+ 2
	79	3.27	1.20	+ 5
	96	3.34	1.15	0
	109	3.39	1.10	-4
	77	3.52	1.15	0
	92	3.36	1.16	+ 1
	85	3.44	1.15	0
ARC	62	3.61	1.18	+ 3
	37	4.01	1.20	+ 4
	67	3.91	1.07	-7
	72	3.26	1.26	+ 10
	54	3.89	1.13	-2
	51	3.90	1.14	-1

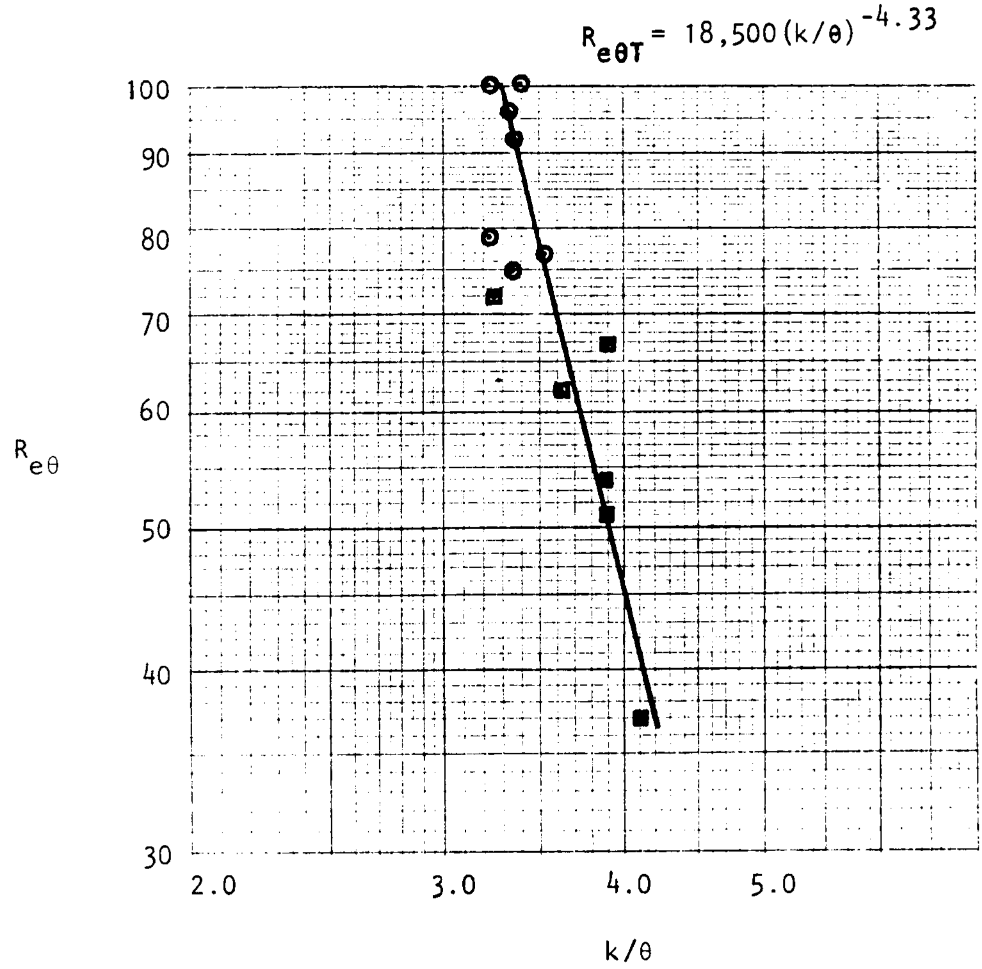

Figure 27. New Correlation and Plotted Data

CHAPTER VII

CONCLUSIONS AND RECOMMENDATIONS

The current study was an intermediate step in fully understanding RV nosetip boundary layer transition, appropriate ground-testing techniques, and their associated correlations. The following conclusions were derived from this study:

1. Modeling RV nosetip boundary-layer transition onset and progression is critical to understand fully nosetip shape change effects on RV performance and accuracy.
2. Of all the past investigators, Batt and Legner [1] performed the most detailed analysis on the boundary layer transition problem and their associated correlation provides good predictions for graphite material and shows promising results for carbon-carbon composites.
3. Both the ballistic-range and the arc-heated wind tunnel are viable testing techniques for measuring boundary layer transition. It was shown that the primary arc tunnel freestream fluctuations are at a significantly lower frequency (250 Hz) than the calculated transition linear-stability frequency (58 kHz).

4. In order to perform accurate ground tests, the nosetip material surface needs to be completely characterized using the probability of exceedance method which was detailed in this paper.
5. The RV nosetip surface temperature doesn't seem to affect the transition correlations as strongly as previous investigators noted.
6. Of the two enthalpies (peak centerline and bulk) measured in the arc tunnel, the peak centerline enthalpy should be used in calculations to determine the flowfield conditions.
7. The current arc-tunnel transition data accurately matched the Batt and Legner correlation.
8. The simplified correlation (not including the wall temperature effects) developed in this study appears to reconcile the differences between the limited arc and range data available on common materials.

Based on the results of this study, the following recommendations are made for the benefit of future studies in the area of RV nosetip boundary layer transition:

1. Further theoretical analysis of the boundary-layer transition problem should be pursued. The Reynolds number approach taken in this study gave

reasonable results, but could be expanded to include many secondary effects.

2. Further testing on carbon-carbon materials should be completed. If a wide variety of material roughnesses could be examined, the new correlation developed in this paper could be refined. Furthermore, actual carbon-carbon nosetips should be tested in hypersonic wind tunnels to evaluate better the transition-temperature effects and the comparisons with early PANT data.
3. Flight-test data should be collected on common materials to be compared to ballistic range and arc tunnel data. This would be a significant step in determining the best ground-test facility and data correlation to be used in the future.
4. The blowing parameter produced by oxidizing and sublimating carbon should be quantified and included in a future correlation.

BIBLIOGRAPHY

BIBLIOGRAPHY

1. Batt, R. G. and Legner, H .H., "A Review of Roughness-Induced Nosetip Transition," AIAA Journal, Vol 21, No. 1, Jan 1983.

2. Berkowitz, A. M., Kyriss, C. L., and Martellucci, A., "Boundary Layer Transition Flight Test Observations," AIAA Paper 77-125, January 1977.

3. Bishop, W. M., "Transition Induced by Distrubuted Roughness on Blunt Bodies in Supersonic Flow," AIAA Paper 77-124, January 1977.

4. Demetriades, A., "Roughness Effects on Boundary Layer Transition in a Nozzle Throat," AIAA Journal, Vol 19, pp. 282-289, March 1981.

5. Dirling, R. B., "The Effect of Transition and Boundary Layer Development on Hypersonic Reentry Shape Change," AIAA Paper 75-673, May 1975.

6. Dirling, R. B., "A Method of Computing Roughwall Heat Transfer Rates on Reentry Nosetips," AIAA Paper 73-763, July 1973.

7. Finson, M. L., "An Analysis of Nosetip Boundary Layer Transition," AFOSR TR-76-1106, August 1976.

8. Keenan, J. H., Gas Tables, John Wiley and Sons, New York, 1980.

9. King, H. C., Muramoto, K. K., Murray, A. L., and Pronchick, S. W., "ABRES Shape Change Code: Technical Report and User's Manual," Acurex Final Report, December 1986.

10. Laderman, A. J., "Effect of Surface Roughness on Blunt Body Boundary Layer Transition," Journal of Spacecraft, Vol 14, No. 4, pp. 253, April 1977.

11. Liepmann, H. W., and Roshko, A., Elements of Gasdynamics, John Wiley and Sons, New York, 1980.

12. Mack, L. M., "Linear Stability Theory and the Problem of Supersonic Boundary Layer Transition," AIAA Journal, Vol 13, No. 3, pp. 278, March 1975.

13. Nestler, D. E., "Pitfalls of Extrapolating Ground Test Data to Hypersonic Reentry Conditions," AIAA 9th Aero Testing Conference.

14. Reda, D. C., "Correlation of Nosetip Boundary Layer Transition Data Measured in Ballistic Range Experiments," Sandia Laboratories SAN79-0649, 1979.

15. Reshotko, E., "Boundary Layer Stability and Transition," Annual Review of Fluid Mechanics, 1976.

16. Saad, M. A., Compressible Fluid Flow, Prentice-Hall, New Jersey, 1985.

17. Schlichting, H., Boundary Layer Theory, McGraw-Hill, New York, 1960.

18. Swigart, R. J., "Roughness Induced Boundary Layer Transition on Blunt Bodies," AIAA Journal, Vol 10, pp. 1355-1356, October 1972.

19. United Technologies, Aeronautical Vestpocket Handbook, Pratt and Whitney Aircraft, 1981.

20. Van Driest, E. R., "Boundary Layer Transition on Blunt Bodies -- Effect of Roughness," AIAA Journal, Vol 5, No. 10, pp. 1913, October 1967.

21. Wassel, A. T., and Courtney, J. F., "Enviromental Characteristics and Experimental Limitations of Arc-Heated Reentry Test Facilities," AFOSR-TR-76-1097, June 1976.

22. White, F. M., Fluid Mechanics, McGraw-Hill, New York, 1979.

23. Wool, M. R., "Summary of Experimental and Analytical Results, Passive Nosetip Technology (PANT) Program," SAMSO-TR-74-86, January 1975.

24. Wright, R. L., and Zoby, E. V., "Flight Boundary Layer Transition Measurements on a slender Cone at Mach 20," AIAA Paper 77-719, June 1977.

25. Wilcox, D. C., "A Model for Transitional Flows," AIAA Paper 77-126, January 1977.

VITA

Robert John Butler was born in Akron, Ohio, on 21 November 1962. He attended elementary schools in the Akron suburb of Coventry and graduated from Coventry High School in June 1981. The following September, he entered Embry-Riddle University in Daytona Beach, Florida, as a four-year USAF ROTC scholarship recipient. In April 1985, he received a Bachelor of Science Degree in Aeronautical Engineering (magna cum laude) and was commissioned in the USAF as a Second Lieutenant.

He was assigned to Arnold Engineering Development Center, Arnold Air Force Base, Tullahoma, Tennessee, in May 1985. Concurrently, he studied at The University of Tennessee Space Institute and received a Master of Science Degree in Aerospace Engineering in May 1989.